

1  
2  
3  
4  
5 **Multidecadal Variability and Predictability**  
6 **of Antarctic Sea Ice in GFDL SPEAR\_LO Model**  
7  
8

9  
10 Yushi Morioka<sup>1,2,3</sup>, Liping Zhang<sup>2,4</sup>, Thomas L. Delworth<sup>2</sup>,  
11 Xiaosong Yang<sup>2</sup>, Fanrong Zeng<sup>2</sup>, Masami Nonaka<sup>1</sup>, Swadhin K. Behera<sup>1</sup>  
12

13 1: Application Laboratory, VAiG, JAMSTEC, Yokohama, Kanagawa, Japan

14 2: Geophysical Fluid Dynamics Laboratory, NOAA, Princeton, New Jersey, USA

15 3: Atmospheric and Oceanic Sciences Program, Princeton University,  
16 Princeton, New Jersey, USA

17 4: University Corporation for Atmospheric Research, Boulder, Colorado, USA  
18

19 July 31, 2023 (Revised)

20 The Cryosphere  
21  
22

23  
24 Corresponding Author: Yushi Morioka

25 Showamachi 3173-25, Kanazawa-ku, Yokohama, JAPAN

26 morioka@jamstec.go.jp, +81-45-778-5509  
27  
28

29 **Abstract**

30 Using a state-of-the-art coupled general circulation model, physical processes underlying  
31 Antarctic sea ice multidecadal variability and predictability are investigated. Our model  
32 simulations constrained by atmospheric reanalysis and observed sea surface temperature  
33 broadly capture the observed sea ice extent (SIE) variability with a low sea ice state (late 1970s-  
34 1990s) and a high sea ice state (2000s-early 2010s), although the model overestimates the SIE  
35 decrease in the Weddell Sea around the 1980s. The low sea ice state is largely due to the  
36 deepening of the mixed layer and the associated deep convection that brings subsurface warm  
37 water to the surface. During the high sea ice period (post-2000s), the deep convection  
38 substantially weakens, so that surface wind variability plays a greater role in the SIE variability.  
39 Decadal retrospective forecasts started from the above model simulations demonstrate that the  
40 Antarctic sea ice multidecadal variability can be skillfully predicted 6-10 years in advance,  
41 showing a moderate correlation with the observation. Ensemble members with a deeper mixed  
42 layer and stronger deep convection tend to predict a larger sea ice decrease in the 1980s,  
43 whereas members with a larger surface wind variability tend to predict a larger sea ice increase  
44 after the 2000s. Therefore, skillful simulation and prediction of the Antarctic sea ice  
45 multidecadal variability require accurate simulation and prediction of the mixed layer, deep  
46 convection and surface wind variability in the model.

47

48 **Keywords**

49 Antarctic sea ice, Multidecadal variability, Predictability, Coupled general circulation model

50

51

## 52 **1. Introduction**

53 Antarctic sea ice plays key roles in exchanging heat, momentum, freshwater, and gases  
54 between the atmosphere and the ocean in the Southern Ocean. Formation of sea ice near the  
55 Antarctic coast generates high-salinity dense water or high-salinity shelf water that flows into  
56 the bottom of the Southern Ocean (e.g., Antarctic Bottom Water; Orsi et al., 1999) and affects  
57 global thermohaline circulation. Antarctic sea ice extent (SIE) undergoes substantial seasonal-  
58 to-interannual variations (e.g., Yuan and Martinson, 2000; Cavalieri et al., 2003), and shows a  
59 slightly increasing trend until 2015 (e.g., Yuan et al., 2017; Parkinson, 2019). This contrasts  
60 with a significant SIE decrease in the early and middle twentieth century, estimated from a  
61 century-long reconstructed SIE data (Fogt et al., 2022). This implies that low-frequency  
62 variability beyond a decadal timescale may exist in the Antarctic SIE. Satellite observation  
63 shows that the Antarctic SIE reaches a record high in 2014 but abruptly declines and reaches a  
64 record low in early 2022 (Simpkins 2023). The Weddell Sea contributes the most to the total  
65 sea ice decrease (Turner et al., 2020). The recent Antarctic SIE decrease is attributed to several  
66 physical processes, including the upper Southern Ocean warming (Meehl et al., 2019; Zhang  
67 et al., 2022b), anomalous warm air advection from the north (Turner et al., 2017) associated  
68 with atmospheric teleconnection from the tropics (Wang et al., 2019), and weakening of the  
69 midlatitude westerlies (Stuecker et al., 2017; Schlosser et al., 2018) linked to a negative phase  
70 of Southern Annual Mode (SAM; Thompson and Wallace, 2000) induced by the weakening of  
71 polar stratospheric vortex (Wang et al., 2019). It is still unclear whether the recent SIE decrease  
72 is a part of interannual or lower-frequency variability or climate change (Eayrs et al., 2021).

73 Most coupled general circulation models (CGCMs) simulate a decreasing trend of the  
74 Antarctic SIE in response to both increasing greenhouse gases and stratospheric ozone  
75 depletion. The positive SIE trend observed in the past three decades until 2015 cannot be solely  
76 explained by anthropogenic forcings, but may be attributed to natural variability (Polvani and  
77 Smith, 2013). For example, Goosse and Zunz (2014) discussed the role of positive ice-ocean  
78 feedback in the amplification of sea ice increase using a CGCM simulation. Once the sea ice  
79 starts to increase, the brine released from the sea ice can be transported downward to deeper  
80 layers and not incorporated back into the mixed layer. This leads to a decrease in the surface  
81 salinity, an increase in the surface stratification, and thus the reduced vertical ocean heat  
82 transport, resulting in a further increase in the sea ice.

83 Open-ocean deep convection (Gordon, 1978; Killworth, 1983; Akitomo et al., 1995) in  
84 the Southern Ocean is also important for Antarctic sea ice variability. For example, Goosse and  
85 Fichet (2001) examined the role of the deep convection in the formation of Weddell polynya

86 (i.e., open water area enclosed by sea ice) using an ocean-ice model. They found that the  
87 surface salinity increase owing to the brine release during the sea ice formation period tends to  
88 induce the deep convection and entrain the relatively warm water from the subsurface ocean to  
89 the surface mixed layer, responsible for the sea ice decrease. The link between the Weddell  
90 polynya and the open-ocean deep convection is widely discussed in the observational and  
91 modeling studies (e.g., Gordon et al., 2007; Cheon et al., 2014, 2015). Recently, Zhang et al.  
92 (2019) pointed out that the observed SST cooling and sea ice increasing trends in the Ross and  
93 Weddell Seas can be reproduced in the CGCM where they start the simulations from an active  
94 phase of the deep convection.

95 On the other hand, surface wind variability also contributes to Antarctic sea ice  
96 variability. Turner et al. (2016) attributed the positive SIE trend in the Ross Sea to stronger  
97 southerly winds associated with a deepening of the Amundsen Sea Low, which are linked to a  
98 negative phase of the Interdecadal Pacific Oscillation (IPO; Power et al., 1999, Meehl et al.,  
99 2016) and a positive phase of the Atlantic Multidecadal Oscillation (AMO; Li et al., 2014).  
100 The stronger southerly winds tend to enhance northward sea ice advection and increase sea ice  
101 concentration in the Ross Sea (Holland and Kwok, 2012). Using a CGCM constrained by  
102 atmospheric reanalysis surface winds and observed SST, Blanchard-Wrigglesworth et al.  
103 (2021) confirmed the influences of surface winds and SST in the Southern Ocean on the  
104 Antarctic SIE trend and variability. However, their simulations could not well reproduce the  
105 low sea ice state in the 1980s and the increasing SIE trend afterwards. Sun and Eisenman (2021)  
106 modified the simulations by replacing the model sea ice velocity with the observed sea ice  
107 motion and found that their new simulations can capture the Antarctic sea ice increasing trend  
108 from 1992 to 2015. The failure of the model in simulating the increasing sea ice trend may be  
109 due to the model biases in the sea ice drift velocity.

110 Several studies have reported skillful predictions of regional and pan-Antarctic SIE  
111 variability at seasonal-to-interannual timescales (Guemas et al., 2014, 2016; Marchi et al.,  
112 2019; Morioka et al., 2019, 2021; Bushuk et al., 2021), and prediction skills of summertime  
113 sea ice are generally lower than those of wintertime sea ice. However, few studies have  
114 examined the multi-year to decadal predictability of the Antarctic SIE. Yang et al. (2016)  
115 provided a broad assessment of the Antarctic SIE predictability using decadal hindcasts from  
116 eleven Coupled Model Intercomparison Project Phase 5 (CMIP5) models. They concluded that  
117 most of the CMIP5 models do not show promising prediction skills for the Antarctic SIE  
118 anomalies. The prediction skills are much lower than the persistence prediction using the  
119 observed SIE anomalies. Most of the CMIP5 models cannot predict the increasing Antarctic

120 SIE trend in the past three decades. When a linear trend is removed from the SIE anomalies,  
121 the prediction skills become higher in the Ross Sea and the Weddell Sea. The prediction skills  
122 in the initialized hindcasts tend to be higher than those in the uninitialized hindcasts. These  
123 results are consistent with a former study (Zunz et al., 2015) that showed a skillful prediction  
124 of the multi-year Antarctic SIE variability by initializing the model surface air temperature.  
125 Recently, Morioka et al. (2022) demonstrated that ocean and sea ice initializations in their  
126 CGCM improve decadal sea ice prediction skills in the west Antarctic Seas. They discussed  
127 the improvement of prediction skills for the regional sea ice, in particular after 2005 when the  
128 subsurface ocean observations increased. However, the model could not capture the sea ice  
129 decrease in the 1980s owing to lack of subsurface ocean observations used for their data  
130 assimilation, so we need further efforts to improve our understanding of multidecadal sea ice  
131 variability and predictability.

132 In this study, we attempt to address the following two scientific questions: what are  
133 relative importance of the Southern Ocean deep convection and the atmospheric variability in  
134 the Antarctic SIE multidecadal variability? How far and skillfully can the Antarctic sea ice  
135 multidecadal variability be predicted and what are the underlying physical processes? To this  
136 end, we examine the Antarctic sea ice multidecadal variability and predictability using the  
137 GFDL (Geophysical Fluid Dynamics Laboratory) newly developed Seamless System for  
138 Prediction and Earth System Research (SPEAR; Delworth et al., 2020) model. We compare  
139 the observation data and model simulations constrained by atmospheric reanalysis surface  
140 winds and temperature and observed SST to evaluate how reasonably the model simulates the  
141 observed SIE variability. We also clarify the relative importance of atmosphere and ocean in  
142 the Antarctic SIE multidecadal variability. Using the decadal retrospective forecasts started  
143 from the above constrained model simulations, we attempt to understand to what extent the  
144 multidecadal sea ice variability can skillfully be predicted. This paper is organized as follows:  
145 Sect. 2 describes the observational data and model experiments performed in this study. In Sect.  
146 3, we provide all the observational and model results. In Sect. 4, we put them into historical  
147 context and discuss the remaining issues to be addressed in future work.

148

## 149 **2. Methodology**

### 150 **2.1. Observation Data**

151 We obtained monthly sea ice concentration (SIC) from the Hadley Centre Global Sea Ice and  
152 Sea Surface Temperature version 1 (HadISST1; Rayner et al., 2003) and version 2 (HadISST2;

153 Titchner and Rayner, 2014) which have a horizontal resolution of one degree. We analyzed the  
154 SIC data during 1958-2020 for HadISST1 and 1958-2019 for HadISST2 to compare with the  
155 SPEAR simulations described below. Since HadISST1 covers a slightly longer period than  
156 HadISST2, we used the SIC data from HadISST1 to perform a persistence decadal  
157 retrospective forecast in which the observed SIC anomaly for each year of 1961-2011 is  
158 assumed to persist over the next 10 years.

159 It should be noted that HadISST2 provides more consistent sea ice record than  
160 HadISST1, because HadISST2 employs new data sources, new bias adjustments, and new  
161 methods to estimate the sea ice concentration based on the sea ice edge information. These  
162 updates lead to higher sea ice concentration and larger extent for some regions and periods in  
163 HadISST2 than HadISST1 (Titchner and Rayner, 2014). Also, both HadISST1 and HadISST2  
164 derive the SIC data indirectly using the monthly climatology of the observations for each  
165 decade before the advent of satellite imagery in 1973. Therefore, the SIC data does not include  
166 any interannual variability before the early 1970s, but gives a general indication of sea ice  
167 variations on decadal timescales. Due to these bias adjustments, HadISST2 tends to show larger  
168 SIE after 1973 than HadISST1 (Titchner and Rayner, 2014). Since there is a large uncertainty  
169 in the SIC data before the satellite period (Hobbs et al., 2016), we discuss physical processes  
170 underlying the multidecadal sea ice variability for the post-satellite (post-1973) period.

171 To compare the sea ice variations obtained from HadISST1 and HadISST2 in the  
172 satellite period, we used another monthly SIC data which are recently released from the  
173 National Oceanic and Atmospheric Administration (NOAA) and the National Snow and Ice  
174 Data Center (NSIDC) (NOAA/NSIDC; Meier et al., 2021). The SIC data from NOAA/NSIDC  
175 is based on the passive microwave data from several satellites and covers a period of 1979-  
176 2020 on the polar stereographic grid with a high resolution of 25 km. We horizontally  
177 interpolated the high resolution SIC data onto HadISST1 data grid. To compare the subsurface  
178 ocean conditions, we used monthly objective analyses of ocean temperature and salinity from  
179 EN4 dataset (Good et al., 2013). For all of these datasets, we calculated monthly anomalies by  
180 removing the monthly climatology and a linear trend using a least squares method.

181

## 182 **2.2 CGCM Experiments**

183 The fully coupled climate model we used in the present study is the SPEAR low  
184 resolution (SPEAR\_LO; Delworth et al., 2020) model. The SPEAR\_LO consists of the AM4  
185 atmospheric and LM4 land surface components (Zhao et al., 2018a, b) and the MOM6 ocean  
186 and SIS2 sea ice components (Adcroft et al., 2019). The atmospheric component of the

187 SPEAR\_LO has a horizontal resolution of approximately 100 km and 33 vertical levels with  
188 the model top at 1 hPa. The ocean and sea ice components have a nominal 1° horizontal  
189 resolution, which increases to 1/3° in the meridional direction toward the tropics. The ocean  
190 model has 75 layers in the vertical which include 30 layers in the top 100 m with a finer  
191 resolution. The ocean model uses a hybrid vertical coordinate which is based on a function of  
192 height in the upper ocean, transitioning to isopycnal layers in the interior ocean. The depth of  
193 transition to isopycnal layers is shallower in the tropics and deeper in the high latitudes (Adcroft  
194 et al., 2019). More details of the SPEAR\_LO are described in a paper by Delworth et al. (2020).

195 The SPEAR\_LO is then partly constrained by observation and reanalysis to mimic more  
196 realistic observational evolutions. Since the ocean observational data, in particular the  
197 subsurface ocean, is relatively sparser than the atmosphere, we nudged the atmospheric model  
198 winds and temperature in all vertical levels to atmospheric reanalysis and the model SST to  
199 observed SST in the SPEAR\_LO decadal coupled initialization/reanalysis system  
200 (SPEAR\_LO\_DCIS; X. Yang et al., 2021). The atmospheric and SST nudging approach allows  
201 the model to generate realistic air-sea fluxes that subsequently drives the ocean (X. Yang et al.,  
202 2021). The SPEAR\_LO\_DCIS covers a period of 1958-2020 and has 30 ensemble members,  
203 starting from ocean, atmosphere, and sea ice conditions in the control simulation with  
204 preindustrial atmospheric radiative forcing, called SPEAR large-ensemble simulation  
205 (SPEAR\_LES; Delworth et al., 2020), at model years 101, 121, 141, and every 20 years  
206 thereafter until model year 681. We find that the model initial years are associated with 14 high  
207 Antarctic SIE years and 16 low SIE years (Supplementary Fig. S1), respectively. Since the  
208 initial years are not in the same phase, our selection of the initial years does not much affect  
209 the simulation of the Antarctic sea ice (c.f., Bushuk et al. 2019). In the SPEAR\_LO\_DCIS, we  
210 nudged the atmospheric model winds and temperature in all vertical levels toward the 6-hourly  
211 atmospheric product from the Japanese 55-year Reanalysis (JRA-55; Kobayashi et al., 2015).  
212 We also nudged the model SST toward the NOAA Extended Reconstructed Sea Surface  
213 Temperature version 5 (ERSSTv5; Huang et al., 2017) data. We applied the SST nudging  
214 within 60°S-60°N at a rate of  $240 \text{ W m}^{-2} \text{ K}^{-1}$ , which corresponds to a 10-day nudging timescale  
215 for a 50-m mixed-layer depth. The strength of SST nudging is tapered linearly from 1.0 at 55°S  
216 (55°N) to 0.0 at 60°S (60°N). Here we nudged the SST within 60°S-60°N, because the ERSSTv5  
217 has a warm bias in the polar region as compared to the satellite observation (Huang et al., 2017)  
218 and this may affect the sea ice distribution and ocean circulation in the model. The  
219 SPEAR\_LO\_DCIS is forced by the time-varying natural and anthropogenic radiative forcing  
220 which is the same as in the SPEAR\_LES. Here we employed a historical forcing for the period

221 of 1958-2014, whereas we adopted a projection forcing with the Shared Socioeconomic  
222 Pathway 5-8.5 (SSP5-8.5) scenario (Kriegler et al., 2017; Riahi et al., 2017) afterwards.  
223 Volcanic aerosol forcing and solar irradiance changes are also included in the model.

224 To examine prediction skills of the Antarctic sea ice multidecadal variability, we also  
225 conducted SPEAR\_LO decadal retrospective forecasts (SPEAR\_LO\_DRF; X. Yang et al.,  
226 2021) starting every 1st January of 1961-2020 from the SPEAR\_LO\_DCIS. We used 20  
227 members of the SPEAR\_LO\_DCIS as the initial conditions and integrated the model without  
228 atmospheric and SST nudging over 10 years with the time-varying natural (e.g., solar  
229 variability and volcanic aerosols) and anthropogenic (e.g., CO2 concentration and aerosols)  
230 radiative forcing based on the observations and developed in support of Coupled Model  
231 Intercomparison Project Phase 6 (CMIP6) Project (Eyring et al., 2016). More details on the  
232 SPEAR\_LO\_DCIS and SPEAR\_LO\_DRF can be seen in a paper written by X. Yang et al.  
233 (2021).

234 To derive monthly anomalies, we removed the monthly climatology and a linear trend  
235 using a least squares method for the SPEAR\_LO\_DCIS. On the other hand, for the  
236 SPEAR\_LO\_DRF, we subtracted a lead-time (i.e., 120 months lead) dependent climatology  
237 (model drift) and linear trend from the output. For example, we calculated monthly climatology  
238 and linear trend for 1-month lead prediction from every January 1st of 1961-2011, then  
239 subtracted them from raw values to calculate the monthly anomalies for 1-month lead  
240 prediction. Removing the linear trend allows us to assess the sea ice prediction skills  
241 originating from natural variability. We also assess the prediction skills by using anomaly  
242 correlation (ACC) between the observation and the model prediction and compare with the  
243 signal-to-noise (S/N) ratio in the model to check whether the model prediction is under-  
244 dispersive and over-confident (Eade et al. 2014; Scaife and Smith 2018),

$$245 \quad S/N = \sqrt{\sigma_{ens}^2 / \sigma_{ind}^2} \quad (1)$$

246 where  $\sigma_{ens}^2$  is the signal variance of the model ensemble mean and  $\sigma_{ind}^2$  is the average variance  
247 of the individual members. The S/N ratio indicates the model skills in predicting itself and if  
248 the S/N ratio is above (below) the ACC, the model prediction is under-dispersive and over-  
249 confident (over-dispersive and under-confident).

250 To gain more insight into possible impacts of atmosphere model resolutions on  
251 representation of the Antarctic sea ice multidecadal variability, we compared two 1000-yr  
252 control simulations forced with atmospheric composition fixed at levels of preindustrial era  
253 between the SPEAR\_LO model and SPEAR medium-resolution (SPEAR\_MED; Delworth et

254 al., 2020) model. The SPEAR\_MED model has a higher atmospheric and land resolution  
255 (approximately 50 km) but has the same ocean and sea ice models with the SPEAR\_LO model.  
256 Details on the differences in simulation of the Southern Ocean multidecadal variability between  
257 the two models are given in a recent paper by Zhang et al. (2022a).

258 We estimated the strength of Southern Ocean deep convection (DCV) by the maximum  
259 absolute value of meridional overturning streamfunction in the density coordinate south of 60°S  
260 (c.f., Zhang et al., 2019) to explore a possible role of Southern Ocean deep convection in the  
261 sea ice variability. We also defined the mixed-layer depth at which the ocean density increases  
262 by 0.03 kg m<sup>-3</sup> from its value at the ocean surface. Furthermore, we evaluated the upper ocean  
263 heat balance using the model output stored at each model grid. In the SPEAR model, the total  
264 ocean heat tendency was calculated by a sum of horizontal advection, vertical advection,  
265 parameterized mesoscale diffusion and diapycnal mixing, and surface heat fluxes.

266

### 267 **3. Results**

#### 268 **3.1 Antarctic Sea Ice Multidecadal Variability Simulated in SPEAR\_LO Model**

269 We show in Fig. 1 the annual mean SIC from HadISST1 and SPEAR\_LO\_DCIS. The  
270 observation (Fig. 1a) shows high SIC above 70 % in the Pacific and Atlantic sectors during  
271 1958-2020. The SPEAR\_LO\_DCIS (Fig. 1b) captures the high SIC in these two regions,  
272 although the simulated SIC is somewhat lower than the observed SIC. Since the monthly  
273 climatology of the Antarctic SIE during austral summer for the SPEAR\_LO\_DCIS  
274 (Supplementary Fig. S2) is lower than the observations, the underestimation of the annual mean  
275 SIC in the SPEAR\_LO model is mostly due to that of the summertime SIC, which is also  
276 reported in other CGCMs contributing to the CMIP6 (Roach et al., 2020). We find a similar  
277 pattern for the satellite period of 1979-2020, although the monthly climatology of the Antarctic  
278 SIC during austral winter for the SPEAR\_LO\_DCIS is higher than that for NOAA/NSIDC  
279 (Supplementary Fig. S2; see also Bushuk et al., 2021).

280 Standard deviation of 5-yr running mean SIC anomalies from the observation (Fig. 1c)  
281 shows a large sea ice variability near the edge of sea ice in the Pacific sector and also near the  
282 coastal region of the eastern Weddell Sea. Here we employed a 5-yr moving average of the  
283 monthly SIC anomalies to extract low-frequency variability with a period longer than 5 years.  
284 The large sea ice variability near the edge of sea ice in the Pacific sector is mostly due to that  
285 during austral autumn-spring (Supplementary Figs. S3c, e, g), while the large sea ice variability  
286 in the coastal region of the eastern Weddell Sea is attributed to that during austral spring-

287 autumn (Supplementary Figs. S3a, c, g). This represents seasonal differences in the decadal  
288 sea ice variability over different regions. The SPEAR\_LO\_DCIS (Fig. 1d) also exhibits a large  
289 sea ice variability in these two regions, but the simulated SIC variability is much larger in the  
290 Weddell Sea. This is mostly due to the larger SIC variability simulated in the eastern Weddell  
291 Sea during austral winter and spring (Supplementary Figs. S3f, h), although the  
292 SPEAR\_LO\_DCIS tends to capture the observed SIC variability there during austral summer  
293 and autumn (Supplementary Figs. S3b, d).

294 In the coastal region of the eastern Weddell Sea, successive polynya events occurred  
295 during the austral winter of 1974-1976 (Carsey, 1980). The Weddell polynya are generated  
296 through various processes (Morales Maqueda et al., 2004) such as the upwelling of deep warm  
297 water as a result of salinity-driven vertical convection (Martinson et al., 1981) and wind-driven  
298 sea ice divergence (Goosse and Fichefet, 2001). Two polynya events are recently reported  
299 during 2016-2017, partly contributing to the record-low sea ice in the Weddell Sea (Turner et  
300 al., 2020). A weaker ocean stratification and increased ocean eddy activities are suggested to  
301 provide favorable conditions for these polynya events (Cheon and Gordon, 2019), although  
302 synoptic atmospheric variability such as polar cyclones and atmospheric rivers may trigger  
303 these events (Francis et al., 2019, 2020). We find that the SPEAR\_LO\_DCIS captures the  
304 negative SIC anomalies associated with these polynya events in the eastern Weddell Sea during  
305 1974-1976 and 2016-2017 (Supplementary Fig. S4), and the simulated amplitudes are weaker  
306 than the observed ones. It is difficult to attribute the 1974-1976 polynya events only to the large  
307 sea ice variability there. There are other reasons for the large sea ice variation in the eastern  
308 Weddell Sea of the SPEAR\_LO\_DCIS, which will be discussed later.

309 Time series of the pan-Antarctic SIE anomalies from the observation (Fig. 2a) show  
310 multidecadal variability with a low sea ice state (late 1970s-1990s) and a high sea ice state  
311 (2000s-early 2010s). A high sea ice state before the early 1970s is also reported in several  
312 studies, including the ones using the satellite images of Nimbus 1 and 2 in the 1960s (Meier et  
313 al., 2013; Gagne et al., 2015), the past 200-yr sea ice edge latitude data reconstructed by ice  
314 core and fast-ice records (J. Yang et al., 2021), and a century-long SIE data reconstructed by  
315 major climate indices (Fogt et al., 2022). However, there is a large degree of uncertainty in the  
316 sea ice data before the satellite period. The SPEAR\_LO\_DCIS exhibits a similar multidecadal  
317 variability and has a significantly high correlation (0.72) with the observed SIE anomalies from  
318 HadISST1. Here we used 12 degrees of freedom to evaluate the statistical significance of the  
319 correlation coefficient, because we applied a 5-yr running mean filter to 63-yr long data. The  
320 model overestimates negative SIE anomalies between the late 1970s and early 1980s (Fig. 2a).

321 This is mostly due to the model overestimation of negative SIE anomalies in the Weddell Sea  
322 (Fig. 2b), and the correlation value with HadISST1 is statistically significant (0.63), slightly  
323 lower than that for the pan-Antarctic SIE. This can also be inferred from the model bias in  
324 capturing the large SIC variability in the Weddell Sea (Fig. 1d).

325 Since the ensemble spreads of the negative SIE anomalies are large, some members (5  
326 out of 30 members) in the SPEAR\_LO\_DCIS are found to produce more reasonable SIE  
327 anomalies over the pan-Antarctic and Weddell Sea as in the observation (Fig. 2a-b). The  
328 ensemble spreads seem to decrease after the late 1990s when the sea ice starts to increase (Fig.  
329 2b). This may be related to different processes controlling the ensemble spreads of the SIE  
330 anomalies before and after the 1990s, which will also be discussed later. Other Antarctic Seas  
331 such as the Ross and Amundsen-Bellingshausen Seas also show a good agreement of the SIE  
332 anomalies between HadISST1 and SPEAR\_LO\_DCIS with significant correlations of 0.50 and  
333 0.84, respectively (Fig. 2c-d). It should be noted that HadISST1 shows larger negative SIE  
334 anomalies in the Amundsen-Bellingshausen Seas between 1980-1985 and larger positive SIE  
335 anomalies after 2010 than NOAA/NSIDC (Fig. 2d). This may be related to the SIC  
336 reconstruction of HadISST1 that uses different sea ice datasets (US National Ice Center, NASA,  
337 and NCEP) before and after the mid-1990s which tend to show higher SIE in the latter period  
338 (Rayner et al., 2003).

339

### 340 **3.2 Physical Processes on the Simulated Antarctic Sea Ice Multidecadal Variability**

341 To explore physical mechanisms underlying the Antarctic sea ice multidecadal  
342 variability in the SPEAR\_LO\_DCIS, we focus on the Weddell Sea (60°W-0°, south of 55°S)  
343 which contributes the most to the total sea ice variability in the SPEAR\_LO\_DCIS (Fig. 2a-b).  
344 Time series of 5-yr running mean wind stress and curl anomalies (Fig. 3a) show that a  
345 significant SIE decrease between the late 1970s and early 1980s is associated with stronger  
346 westerlies and negative wind stress curl anomalies. These surface wind anomalies tend to  
347 induce anomalous upwelling of warm water from the subsurface ocean on decadal and longer  
348 timescales (Ferreira et al., 2015), contributing to the sea ice decrease. The westerly and  
349 negative curl anomalies coincide with a positive phase of the SAM (Fig. 3b), although  
350 ensemble spreads of the SAM index (Gong and Wang, 1999) are relatively large except some  
351 periods (early 1960s, late 1970s, and early 1990s). The IPO index (Fig. 3b), which is defined  
352 as the 13-yr running mean of the SST tripole index in the tropics and subtropics (Henley et al.,  
353 2015), is negative around 1975 when the westerly and negative curl anomalies start to appear,  
354 but turns to positive values after 1980. This out-of-phase relationship indicates that the surface

355 wind variability in the Weddell Sea is more related to the SAM than the IPO. On the other  
356 hand, the net surface heat flux (Fig. 3c) shows negative (upward) anomalies between the late  
357 1970s and early 1980s. As a result of the decrease in sea ice, more heat is released from the  
358 ocean surface. We obtain an opposite but similar process for the high sea ice state after the  
359 2000s when weaker westerlies and positive wind stress curl anomalies appear. These wind  
360 anomalies are found to have almost the same amplitude as those in the low sea ice period. This  
361 implies that the surface wind variability cannot fully explain the large negative SIE anomalies  
362 in the SPEAR\_LO\_DCIS during the late 1970s and early 1980s.

363         The substantial SIE decrease between the late 1970s and the early 1980s is associated  
364 with positive SST anomalies (Fig. 3d). A positive peak of the SST anomalies in the early 1980s  
365 is associated with a positive peak of the mixed layer depth anomalies followed by that of the  
366 deep convection anomalies. The deepening of the mixed layer and the associated deep  
367 convection tend to entrain more warm water from the subsurface ocean. This plays a crucial  
368 role in the development of extremely low sea ice in the Weddell Sea. Moreover, the negative  
369 SIE anomalies are accompanied by positive sea surface salinity (SSS) anomalies (Fig. 3e). Net  
370 salt flux into the ocean at the surface associated with sea ice formation shows positive  
371 anomalies, but the amplitude is much smaller than positive anomalies of the precipitation minus  
372 evaporation corresponding to net surface water flux into the ocean. As a result of the decrease  
373 in sea ice, more freshwater goes into the ocean, but this cannot explain the SSS increase in the  
374 Weddell Sea. Rather, the SSS increase is driven by other oceanic processes, that is, the deeper  
375 mixed layer and the associated deep convection that entrain relatively high salinity water from  
376 the subsurface ocean.

377         To highlight a possible role of subsurface ocean variability, we describe time series of  
378 ocean temperature and salinity anomalies averaged in the Weddell Sea as a function of depth  
379 (Fig. 4). Observation data (Fig. 4a) shows that sea ice decrease between the late 1970s and  
380 early 1980s is accompanied by positive temperature anomalies in the upper 200 m and negative  
381 temperature anomalies below 200 m. The SPEAR\_LO\_DCIS (Fig. 4b) captures this dipole  
382 structure of the positive and negative temperature anomalies, although the amplitude is much  
383 larger than that in the observation. Interestingly, both the observation and SPEAR\_LO\_DCIS  
384 (Fig. 4a-b) show that the positive temperature anomalies in the upper 200 m start to appear in  
385 the early 1970s and are preceded by positive temperature anomalies below 200 m in the 1960s,  
386 although the SPEAR\_LO\_DCIS has uncertainty in simulation of the subsurface temperature  
387 anomalies in the Weddell Sea during the early 1960s because of the slow oceanic response to  
388 the prescribed atmospheric forcing since 1958. The anomalous heat buildup in the subsurface

389 ocean during the 1960s may have links to the subsequent surface warming in the 1970s. On the  
390 other hand, the salinity anomalies between the late 1970s and the early 1980s are positive in  
391 the upper 200 m and negative below 200 m for both the observation (Fig. 4c) and  
392 SPEAR\_LO\_DCIS (Fig. 4d). Since both the temperature and salinity anomalies exhibit the  
393 dipole structure in the vertical, vertical ocean processes are expected to operate for inducing  
394 these anomalies.

395 The observed ocean density shows positive anomalies from the surface to the deeper  
396 ocean around 1980 (Fig. 5a). The SPEAR\_LO\_DCIS also shows the higher density around  
397 1980, although the amplitude is larger than the observation (Fig. 5b). Associated with the  
398 positive density anomalies, the mixed layer anomalously deepens. The observed ocean  
399 stratification, which is estimated by squared Brunt Väisälä frequency, shows negative  
400 anomalies in the upper 200 m around 1980. (Fig. 5c). The SPEAR\_LO\_DCIS also shows  
401 weaker stratification (Fig. 5d), which starts to appear below 100 m in the 1960s and provides  
402 favorable conditions for deepening of the mixed layer. We decomposed the density anomalies  
403 into the anomalies solely dependent on temperature anomalies and other ones accompanied by  
404 salinity anomalies. We find that the negative density anomalies below 200 m in the 1960s are  
405 driven by the warm temperature anomalies (Figs. 4b, 5e), whereas the positive density  
406 anomalies in the upper 200 m during the late 1970s and early 1980s arise from those associated  
407 with the positive salinity anomalies (Figs. 4d, 5f). Both the subsurface heat buildup and the  
408 surface salinity increase contribute to the deepening of the mixed layer from the 1960s to the  
409 early 1980s that results in warmer SST and sea ice decrease.

410 To further investigate how the surface temperature and salinity anomalies are generated,  
411 we evaluated ocean heat and salinity tendency anomalies in the upper 200 m (Fig. 6). Here we  
412 combine both contributions from the diapycnal mixing and mesoscale diffusion into one term,  
413 because the contribution from the mesoscale diffusion is found to be much smaller than that  
414 from the diapycnal mixing. The heat tendency anomalies in the upper 200 m (Fig. 6a) are  
415 positive in the late 1970s and early 1980s when the positive SST and negative SIE anomalies  
416 develop (Fig. 3d). The positive heat tendency anomalies are mostly due to the vertical  
417 advection, although they are partly contributed by the vertical mixing and horizontal advection.  
418 Similarly, the positive salinity tendency anomalies in the upper 200m during the period are  
419 mostly explained by the vertical advection. These results indicate that the deepening of mixed  
420 layer (Fig. 3d) entrains more warm and saline water from below the mixed layer to increase  
421 the ocean temperature and salinity at surface. We obtain a similar but opposite process for

422 negative temperature tendency anomalies after the late 1990s when the positive SIE anomalies  
423 develop (Fig. 3d).

424

### 425 **3.3 Ensemble Spreads of the Simulated Antarctic Sea Ice Multidecadal Variability**

426 We have so far discussed physical processes for ensemble mean fields of the  
427 SPEAR\_LO\_DCIS, but this analysis does not provide any explanation for the ensemble  
428 spreads representing model uncertainty. To explore the underlying causes of ensemble spreads  
429 in a simple way, we performed inter-member correlation analysis for 30 ensemble members of  
430 the SPEAR\_LO\_DCIS. Here we calculated the correlation between the anomalies of SIE and  
431 other variables simulated from the 30 ensemble members, assuming that initial differences in  
432 the anomalies of other variables lead to those in the SIE anomalies. Figure 7a shows time series  
433 of inter-member correlation coefficients between the 5-yr running mean SIE anomalies and the  
434 leading zonal wind stress anomalies in the Weddell Sea as a function of lead years. Zonal wind  
435 stress anomalies have significantly large negative correlations with SIE anomalies by 3-4 lead  
436 years during the 1970s and the 1980s when the sea ice anomalously decreases. This means that  
437 ensemble members with stronger westerlies than the ensemble mean tend to simulate larger  
438 sea ice decrease 3-4 years later. We find weakly positive correlations in around 1980s with  
439 lead times longer than 6 years, but these cannot explain the sea ice decrease because the weaker  
440 westerlies tend to suppress upwelling of warm water from the subsurface and contribute to sea  
441 ice increase. The negative correlations with the zonal wind stress become stronger with longer  
442 lead times after the late 1990s when the sea ice anomalously increases. This represents more  
443 influence of weaker westerlies on the anomalous sea ice increase. We obtain similar but  
444 opposite correlations between the SIE anomalies and the leading wind stress curl anomalies  
445 (Fig. 7b). Ensemble members with more negative wind stress curl anomalies than the ensemble  
446 mean tend to simulate larger sea ice decrease in the 1970s and the 1980s, and vice versa after  
447 the late 1990s.

448 Inter-member correlations between the SIE anomalies and the leading MLD anomalies  
449 (Fig. 7c) show significantly large and negative values by 3-4 lead years in the 1970s and the  
450 1980s and by 5-6 lead years after the late 1990s. This indicates that ensemble members with  
451 deeper mixed layer than the ensemble mean tend to simulate larger sea ice decrease 3-4 years  
452 later in the 1970s and the 1980s, whereas the members with shallower mixed layer than the  
453 ensemble mean tend to simulate larger sea ice increase 5-6 years later after the late 1990s. It  
454 should be noted that we used spatially averaged values over the whole Weddell Sea ( $60^{\circ}\text{W}-0^{\circ}$ ),  
455 so the results also include the destratified process near the coast dominated by sea ice

456 production. However, the SIE variability in the Weddell Sea is pronounced in the open water  
457 (Fig. 1d), so the results mostly represent the open-water stratified process of cold/fresh water  
458 over warm/salty circumpolar deep water. Similarly, we find negative correlations between the  
459 SIE anomalies and the 1-2 yr leading deep convection anomalies (Fig. 7d), but the links with  
460 the deep convection are much weaker than the mixed layer. Therefore, the large uncertainty in  
461 the simulated amplitude of the mixed layer contributes more to that in the sea ice decrease in  
462 the late 1970s and 1980s, while the model uncertainty in the surface wind variability  
463 contributes more to that in sea ice increase after the late 1990s (Fig. 7a-c).

464

### 465 **3.4 Skillful Prediction of Antarctic Sea Ice Multidecadal Variability**

466 For quantitative assessment of prediction skills of the Antarctic sea ice multidecadal  
467 variability, we first calculated anomaly correlations (ACCs) of the 5-yr mean SIC anomalies  
468 for the persistence prediction using the observed SIC anomalies from HadISST1 (Figs. 8a, b).  
469 Here we used 50 degrees of freedom to evaluate statistical significance of the ACC, because  
470 we performed decadal reforecasts independently starting from each year of 1961-2011.  
471 Persistence prediction shows very limited prediction skills of the sea ice variability in the  
472 Antarctic seas at a lead time of 1-5 years (Fig. 8a). The ACCs significantly drop below zero at  
473 a lead time of 6-10 years (Fig. 8b), indicating that the observed SIC anomalies cannot persist  
474 beyond five years. This can also be seen in the year-to-year ACCs (Supplementary Fig. S5)  
475 that shows the highest values in lead year 1, quickly decay in lead year 2, then vanish afterward.

476 To compare with the persistence prediction skills, we calculated the ACCs between the  
477 5-yr mean observed SIC anomalies and the ensemble mean (i.e., simple average of 20  
478 members) of the predicted SIC anomalies from the SPEAR\_LO\_DRF for the prediction lead  
479 times of 1-5 yr and 6-10 yr, separately (Figs. 8c, d). For example, in the case of 1-5 yr lead  
480 prediction for the targeted observation period of 2010-2014, we used the predicted anomalies  
481 starting from 2005-2009 to 2009-2013, respectively. The ACCs in the SPEAR\_LO\_DRF are  
482 significantly high at a lead time of 1-5 years (Fig. 8c), as compared to the persistence prediction  
483 (Fig. 8a). In particular, the ACCs become higher in the Amundsen-Bellingshausen Seas,  
484 Weddell Sea, and Indian sector. These regions well correspond to those with higher ACCs of  
485 the SST in the model (see Fig. 10 in X. Yang et al., 2021), indicating a close relationship  
486 between the SIC and SST variations. The ACCs in these regions become smaller but remain  
487 significant for a lead time of 6-10 years (Fig. 8d).

488 The high ACCs at a lead time of 1-5 years are mostly due to those during austral  
489 autumn-spring (Supplementary Fig. S6c, e, g), while the significant ACCs at a lead time of 6-

490 10 years are mainly attributed to those during austral winter and spring (Supplementary Fig.  
491 5f, h). Decadal sea ice predictability during austral summer (Supplementary Fig. S6a-b) is the  
492 lowest, because the sea ice extent reaches its minimum and the decadal SIC variability is  
493 confined near the Antarctic coast occupying smaller areas (Supplementary Fig. S3a). We can  
494 also find that the year-to-year prediction skills of the ACC from the SPEAR\_LO\_DRF  
495 (Supplementary Fig. S7) are higher than those from the persistence prediction (Supplementary  
496 Fig. S5), although the amplitude of the ACC (Supplementary Fig. S7) is lower than the  
497 prediction skills of 5-yr mean SIC (Fig. 8c-d) probably due to large interannual variations of  
498 the Antarctic SIC.

499 To further demonstrate the spatio-temporal evolution of prediction skills in the  
500 SPEAR\_LO\_DRF, we calculated the ACCs of the 5-yr area-weighted mean SIC anomalies in  
501 the pan-Antarctic region and the Weddell Sea as a function of lead times (Fig. 9a-b). The ACCs  
502 of the pan-Antarctic SIC anomalies in the SPEAR\_LO\_DRF are significantly higher than those  
503 in the persistence prediction for any lead times from 1-5 years to 6-10 years (Fig. 9a). A few  
504 ensemble members have low ACCs comparable to the persistence prediction, but the ACCs of  
505 the ensemble mean SIC anomalies are high at around 0.4-0.6. We also find that the ACCs are  
506 relatively high compared to the average of the individual ACCs. The S/N ratio in the model  
507 also exceeds the ACCs of the ensemble mean. These results indicate that the model prediction  
508 is under-dispersive and over-confident. We obtain similar results for the ACCs of the SIC  
509 anomalies in the Weddell Sea (Fig. 9b), but the ACCs become insignificant after a lead time  
510 of 6-10 years. Overall, the ACCs in the Weddell Sea are lower than those in the pan-Antarctic  
511 region.

512 Since the ACCs do not evaluate skills for the amplitude of the predicted anomalies, we  
513 plotted time series of the 5-yr running mean SIC anomalies in the pan-Antarctic region and the  
514 Weddell Sea for different lead times from 1-5 years to 6-10 years (Fig. 9c-d). The  
515 SPEAR\_LO\_DRF better captures the observed SIC anomalies in the pan-Antarctic region than  
516 the Weddell Sea (Fig. 9c-d). As the lead times increase, the amplitude of the predicted  
517 anomalies decreases and gets closer to the observation, particularly during the 1980s (Fig. 9c-  
518 d). Since the time series of the predicted anomalies for the 1-5 year leads resembles that of the  
519 initial sea ice anomalies in the model (Fig. 2a-b), the influence of the Southern Ocean deep  
520 convection initialized in the model during the 1980s remains stronger for the earlier lead times,  
521 as will be discussed below, causing larger differences in the observed and predicted amplitudes.  
522 The predicted SIC anomalies return to neutral at around 2000 and become positive afterwards,  
523 although the model underestimates the positive SIC anomalies observed in the early 2010s. We

524 find similar results for the Antarctic SIC anomalies normalized by standard deviation, but the  
525 predicted amplitude gets closer to the observation (Fig. S8a). For the SIC anomalies in the  
526 Weddell Sea (Figs. 9d, S8b), the observed anomalies largely fluctuate on a shorter timescale,  
527 so the model cannot capture positive SIC anomalies in the early 1990s and negative SIC  
528 anomalies in the mid-1970s and late 1990s.

529

### 530 **3.5 Potential Sources of Antarctic Sea Ice Multidecadal Predictability**

531 The temporal evolution of the pan-Antarctic SIC anomalies in the SPEAR\_LO\_DRF  
532 (Fig. 10a) shows that positive and negative SIC anomalies predicted at a lead time of 1-5 years  
533 tend to persist over five years up to a lead time of 6-10 years. Negative SIC anomalies predicted  
534 in the 1980s for a lead time of 1-5 years gradually weaken as the lead time increases, but remain  
535 the same in the late 1980s and early 1990s for a lead time of 6-10 years. The negative SIC  
536 anomalies in the late 1980s and early 1990s for a lead time of 6-10 years are associated with  
537 positive zonal wind anomalies and negative meridional wind anomalies (Fig. 10b-c). The  
538 stronger westerlies act to induce northward Ekman current anomalies on interannual and  
539 shorter timescales, but on decadal and longer timescales, the associated upwelling of warm  
540 water from the subsurface ocean tends to reduce the SIC (Ferreira et al., 2015). Also, the  
541 northerly anomalies contribute to the SIC decrease by bringing more warm air from the north  
542 during the period. The wind stress curl (Fig. 10d) shows positive anomalies in the 1980s for a  
543 lead time of 1-5 years and also in the late 1980s and early 1990s for a lead time of 6-10 years.  
544 However, the positive wind stress curl anomalies tend to weaken the upwelling of warm water  
545 from the subsurface ocean and decrease the upper ocean temperature. This is inconsistent with  
546 sea ice decrease during that period.

547 The westerly anomalies in the late 1980s and early 1990s for a lead time of 6-10 years  
548 are associated with a positive phase of the SAM (Fig. 10e), while the IPO index changes from  
549 the positive to negative values (Fig. 10f). The closer link of the surface wind variability with  
550 the SAM is consistent with the previous discussion in the Weddell Sea (Fig. 3b). The net  
551 surface heat flux (Fig. 10g) also shows negative anomalies in the 1980s and early 1990s for all  
552 lead times. This represents more heat release from the ocean surface as a result of the sea ice  
553 decrease. We obtain similar but opposite processes for the positive SIC anomalies after the  
554 2000s.

555 To elucidate a potential role of ocean variability, we plotted temporal evolution of 5-yr  
556 running mean anomalies of predicted ocean variables (Fig. 11). The Southern Ocean SST (Fig.  
557 11a) shows positive anomalies in the 1980s for a lead time of 1-5 years and in the late 1980s

558 and early 1990s for a lead time of 6-10 years. This represents persistence of the predicted SST  
559 anomalies over five years. The positive SST anomalies are strongly accompanied by positive  
560 mixed-layer depth anomalies in the 1980s (Fig. 11c) and positive deep convection anomalies  
561 in the late 1980s (Fig. 11e) for lead times between the 1-5 years and 3-7 years. As explained  
562 earlier, the deepening of the mixed layer and the associated deep convection contribute to the  
563 positive SST anomalies by entraining warm water from the subsurface ocean into the surface  
564 mixed layer.

565 During that period, SSS anomalies (Fig. 11b) are positive in association with the  
566 slightly positive anomalies of the net salt flux into the ocean (Fig. 11d). Precipitation minus  
567 evaporation corresponding to the net surface water flux into the ocean (Fig. 11f) shows slightly  
568 negative anomalies. This represents more evaporation from the ocean surface as a result of sea  
569 ice decrease. Given that the amplitude of the freshwater flux anomalies is much larger than the  
570 salt flux anomalies, the evaporation from the ocean surface contributes partly to the SSS  
571 increase in the 1980s. In addition to the effect of surface evaporation, the deepening of the  
572 mixed layer and the associated deep convection help increase the SSS during that period. We  
573 obtain similar but opposite processes for the sea ice increase after the 2000s. More freshwater  
574 input (Fig. 11f) and anomalous heat input (Fig. 10g) into the surface mixed layer may  
575 contribute to the shallower mixed layer. This indicates more active roles of atmosphere-ocean  
576 interaction at the surface than the subsurface ocean variability.

577 To further examine possible links with atmosphere and ocean variability among  
578 ensemble members, we calculated the temporal evolution of inter-member correlations  
579 between the SIC anomalies for a lead time of 6-10 years and the SST anomalies for each lead  
580 time from 1-5 years to 6-10 years (Fig. 12a). For example, the correlation coefficient in 1980  
581 with a lead time of 1-5 years is the one between the SIC anomalies predicted in 1986-1990 and  
582 the SST anomalies predicted in 1981-1985. The SIC anomalies predicted at a lead time of 6-  
583 10 years show significantly negative correlations with the SST anomalies in the 1980s for a  
584 lead time of 1-5 years. This means that ensemble members with larger positive SST anomalies  
585 in the 1980s tend to predict larger negative SIC anomalies five years later. Zonal and  
586 meridional wind stress anomalies (Fig. 12b-c) show significantly negative and positive  
587 correlations with the SIC anomalies, respectively, as expected from the ensemble mean results  
588 (Fig. 10b-c). However, the links with the wind stress curl anomalies (Fig. 12d) are much weaker.

589 On the other hand, the mixed-layer depth and deep convection anomalies in the 1980s  
590 (Fig. 12e-f) show significantly negative correlations with the SIC anomalies for a lead time of  
591 6-10 years, although the deep convection shows a weaker correlation than the mixed layer

592 depth. This indicates that ensemble members with a deeper mixed layer and stronger deep  
593 convection than the ensemble mean tend to predict a larger sea ice decrease and vice versa.  
594 However, the links with deep convection becomes weaker after the 2000s when the sea ice  
595 anomalously increases. These results suggest that subsurface ocean variability contributes to  
596 skillful and long lead-time prediction of sea ice decrease in the 1980s, while atmosphere-ocean  
597 interaction at the surface plays more important roles in predicting sea ice increase after the  
598 2000s.

599

#### 600 **4. Summary and Discussion**

601 This study has examined the relative importance of the Southern Ocean deep  
602 convection and surface winds in the Antarctic sea ice multidecadal variability and predictability  
603 using the GFDL SPEAR\_LO model. Observed SIE anomalies show a multidecadal variability  
604 with a low sea ice state (late 1970s-1990s) and a high sea ice state (2000s-early 2010s). The  
605 increasing SIE trend from the late 1990s to the early 2010s is reported in many studies (e.g.,  
606 Yuan et al. 2017; Parkinson 2019), and this is in contrast to a significant SIE decrease in the  
607 early and middle twentieth century, estimated from century-long SIE reconstructed data (Fogt  
608 et al. 2022). These results suggest that a low-frequency variability beyond a decadal timescale  
609 exists in the Antarctic SIE.

610 When the SPEAR\_LO model is constrained with atmospheric reanalysis winds and  
611 temperature and observed SST (i.e., SPEAR\_LO\_DCIS), the model reproduces the overall  
612 observed multidecadal variability of the Antarctic SIE. The broad SIE decrease in the Southern  
613 Ocean from the late 1970s to the 1990s mainly occurred in the Weddell Sea. This is driven by  
614 the deepening of the mixed layer and the associated deep convection in the Southern Ocean  
615 that brings subsurface warm water to the surface. The role of subsurface ocean variability has  
616 not been well explored in previous studies on the Weddell Sea decadal variability (Venegas  
617 and Drinkwater, 2001; Hellmer et al., 2009; Murphy et al., 2014; Morioka and Behera, 2021).  
618 We have also demonstrated that the deeper mixed layer and the associated deep convection  
619 simulated in the model are important for the skillful prediction of the Antarctic sea ice decrease  
620 from the late 1970s to the 1990s. Ensemble members with the deeper (shallower) mixed layer  
621 and stronger (weaker) deep convection than the ensemble mean tend to predict the higher  
622 (lower) SST and larger (smaller) sea ice decrease in the 1980s. Our results are in good  
623 agreement with a previous study by Zhang et al., (2019). They have demonstrated that a gradual  
624 weakening of the deep convection in their CGCM simulation initiated from an active phase of

625 the deep convection is the key to a realistic representation of the Southern Ocean cooling and  
626 the associated Antarctic SIE increase in recent decades.

627 It should be noted that our model prediction is under-dispersive and over-confident.  
628 This may be related to a small number of ensemble members, a lack of ensemble spread, and  
629 systematic errors in predicted signals (Eade et al. 2014, Scaife and Smith 2018). Also, the  
630 results presented here can be model dependent. SPEAR\_LO\_DRF shows similar prediction  
631 skills with the other model (SINTEX-F2; see Fig. 1f in Morioka et al. 2022), but the prediction  
632 skills in the Indian sector is higher (Fig. 8d). SPEAR\_LO employs the SST and atmospheric  
633 initializations since the 1960s, while SINTEX-F2 uses the SST, sea ice cover and subsurface  
634 ocean temperature/salinity initializations since the 1980s (Morioka et al. 2022). However, it is  
635 difficult to directly compare the model prediction skills and discuss the reasons for the  
636 differences because of large differences in the model physics, initialization schemes and  
637 hindcast periods between the two models. We need further comparison studies using different  
638 models with the same initialization schemes and hindcast periods.

639 The SPEAR\_LO\_DCIS well captures the observed multidecadal variability of the  
640 Antarctic SIE (Fig. 2), but overestimates the SIE decrease in the Weddell Sea around the 1980s  
641 (Fig. 2b). In the 1970s, the Weddell Sea experienced three consecutive polynya events during  
642 austral winters between 1974 and 1976 in observations. Strengthening of westerly winds and  
643 the associated stronger deep convection bring more warm water to the surface and cause  
644 significant sea ice loss in the Weddell Sea (Cheon et al., 2014, 2015). Since the model is  
645 constrained by atmospheric reanalysis winds and temperature and observed SST, the  
646 overestimation of the SIE decrease in the Weddell Sea is attributed to that of the deep  
647 convection in the model. In fact, the simulated ocean temperature anomalies in the  
648 SPEAR\_LO\_DCIS (Fig. 4b) are larger than the observed temperature anomalies (Fig. 4a),  
649 although the observed temperature may have some uncertainty due to an insufficient number  
650 of subsurface ocean observations. Consistently, ensemble members with a weaker deep  
651 convection than the ensemble mean tend to capture a smaller SIE decrease than that observed  
652 in the Weddell Sea (Fig. 2b). Therefore, realistic simulation of the Southern Ocean deep  
653 convection is the key for reproducing the Antarctic SIE decrease from the late 1970s.

654 The use of convective models may be helpful for accurate simulation and prediction of  
655 the SIE decrease in the 1980s and the increasing SIE trend afterwards. For example, using a  
656 ‘non-convective’ CGCM that cannot simulate open water deep convection in the Southern  
657 Ocean where the wintertime mixed-layer depth exceeds 2000 m (de Laverage et al., 2014),  
658 Blanchard-Wrigglesworth et al. (2021) demonstrated that even with the surface winds and SST

659 initializations in the Southern Ocean, the model could not reproduce the Antarctic SIE decrease  
660 in the 1980s and did not well capture the increasing SIE trend afterwards. They have suggested  
661 that the results may be conditioned by the feature of the model that does not simulate the deep  
662 convection in the Southern Ocean, while some of the model failure in simulating the increasing  
663 sea ice trend may be due to the model biases in the sea ice drift velocity (Sun and Eisenman  
664 2021). Therefore, in this study, we used the SPEAR\_LO model that is classified as a  
665 ‘convective’ model (de Laverage et al., 2014) to demonstrate the role of deep convection in the  
666 low-frequency sea ice variability.

667 A recent study by Zhang et al. (2022a) has reported that the SPEAR\_MED model  
668 (Delworth et al., 2020) with a higher atmospheric resolution tends to simulate a weaker deep  
669 convection variability in the Southern Ocean than the SPEAR\_LO model. The standard  
670 deviation of 5-yr running mean SIC anomalies from the 1000-yr SPEAR\_LO control  
671 simulation (SPEAR\_LO\_CTL) with the preindustrial atmospheric radiative forcing (Fig. 13a)  
672 is larger in the Pacific and Atlantic sectors than that from the SPEAR\_MED control simulation  
673 (SPEAR\_MED\_CTL; Fig. 13b). This makes the SIC variability in the SPEAR\_MED\_CTL  
674 closer to the observed one (Fig. 1c) and appears to have links to smaller mixed-layer depth  
675 variability in the SPEAR\_MED\_CTL (Fig. 13d) than in the SPEAR\_LO\_CTL (Fig. 13c). The  
676 weaker deep convection variability in the SPEAR\_MED\_CTL appears to contribute to the  
677 weaker mixed-layer variability and hence the weaker sea ice variability. Decadal reforecasts  
678 using the SPEAR\_MED model may demonstrate more reasonable prediction skills of the  
679 Antarctic sea ice low-frequency variability than those using the SPEAR\_LO model.  
680 Furthermore, the increase in the ocean resolution may help better represent the mean state and  
681 variability of the Southern Ocean which involves rich mesoscale eddies (Hallbert et al. 2013)  
682 thereby improving the decadal predictions, but this is beyond the scope of this study.

683 This study has further identified that the Southern Ocean deep convection gradually  
684 weakens after the 1990s and the surface wind variability starts to play a greater role in the  
685 Antarctic SIE increase after the 2000s. Weakening of the deep convection may be attributed to  
686 both an internal Southern Ocean multidecadal variability (Zhang et al., 2021) and a surface  
687 freshening owing to anthropogenic forcing (de Lavergne et al., 2014). On the other hand, more  
688 frequent occurrence of a positive phase of the SAM tends to strengthen the westerly winds and  
689 induce northward transport of cold water and sea ice, leading to the Antarctic sea ice increase  
690 at a shorter timescale (e.g., J. Yang et al., 2021; Crosta, 2021). In addition, the southerly wind  
691 anomalies associated with the deepening of the Amundsen Sea Low assist in bringing more  
692 cold air from the Antarctica and enhancing sea ice formation in the Ross Sea (Turner et al.,

693 2016; Meehl et al., 2016). Although the sources of decadal predictability remain unclear,  
694 skillful prediction of the Antarctic SIE increase after the 2000s, which is not well reproduced  
695 in most of the CMIP5 models (Polvani and Smith, 2013; Yang et al., 2016), requires better  
696 representation of atmospheric circulation variability as well as ocean and sea ice variability in  
697 the Southern Ocean (Morioka et al., 2022).

698 The Antarctic SIE has experienced a slightly increasing trend over the past decades  
699 (Yuan, 2017; Parkinson, 2019). However, it has suddenly declined since 2016 and reached a  
700 record low in early 2022 (Simpkins 2023). Several studies attributed the recent sea ice decrease  
701 to various factors including the upper Southern Ocean warming (Meehl et al., 2019; Zhang et  
702 al., 2022b), the anomalous warm air advection from the north (Turner et al. 2017; Wang et al.  
703 2019), and the weakening of the midlatitude westerlies (Stuecker et al., 2017; Schlosser et al.,  
704 2018; Wang et al., 2019). However, it is unclear whether the sea ice decrease reflects an  
705 interannual or low-frequency variability or climate change (Eayrs et al., 2021), owing to a short  
706 observation record. We need to wait for this to be verified using more observational data when  
707 it becomes available in the future.

708

## 709 **Code Availability**

710 All codes to generate the figures can be provided upon the request to the corresponding author.

711

## 712 **Data Availability**

713 Monthly SIC data from HadISST1 and HadISST2 can be obtained from here:  
714 <https://www.metoffice.gov.uk/hadobs/hadisst/data/download.html> and  
715 <https://www.metoffice.gov.uk/hadobs/hadisst2/data/download.html>, respectively. Another  
716 monthly SIC data from the NOAA/NSIDC Climate Data Record website is also available here:  
717 <https://nsidc.org/data/G02202/versions/4>. Monthly ocean temperature and salinity data are  
718 downloaded from the EN4 website: <https://www.metoffice.gov.uk/hadobs/en4/download.html>.

719

## 720 **Author Contributions**

721 Y. M. performed data analysis and wrote the first draft of the manuscript, while L. Z. provided  
722 the reconstructed data and X. Y. and F. Z. performed the model experiments. All authors  
723 commented on previous versions of the manuscript and approved the final manuscript.

724

## 725 **Competing Interests**

726 The authors declare that they have no conflict of interest.

727

## 728 **Acknowledgments**

729 We performed all of the SPEAR model experiments on the Gaea supercomputer at NOAA. We  
730 thank Drs. Rong Zhang, Mitch Bushuk, Yongfei Zhang and William Gregory for providing  
731 constructive comments on the original manuscript. We are also grateful to two anonymous  
732 reviewers who provided valuable comments to improve the original manuscript. The present  
733 research is supported by Princeton University/NOAA GFDL Visiting Research Scientists  
734 Program and base support of GFDL from NOAA Office of Oceanic and Atmospheric Research  
735 (OAR), JAMSTEC Overseas Research Visit Program, JSPS KAKENHI Grant Number  
736 19K14800 and 22K03727.

737

738 **References**

- 739 Akitomo, K., Awaji, T., and Imasato, N: Open-ocean deep convection in the Weddell Sea:  
740 Two-dimensional numerical experiments with a nonhydrostatic model, *Deep Sea Res. Part I*,  
741 42, 53-73, [https://doi.org/10.1016/0967-0637\(94\)00035-Q](https://doi.org/10.1016/0967-0637(94)00035-Q), 1995.
- 742
- 743 Adcroft, A., Anderson, W., Balaji, V., Blanton, C., Bushuk, M., Dufour, C. O., et al.: The  
744 GFDL global ocean and sea ice model OM4.0: Model description and simulation features, *J.*  
745 *Adv. Mod. Ear. Sys.*, 11, 3167–3211, <https://doi.org/10.1029/2019MS001726>, 2019.
- 746
- 747 Blanchard-Wrigglesworth, E., Roach, L. A., Donohoe, A., and Ding, Q.: Impact of winds and  
748 Southern Ocean SSTs on Antarctic sea ice trends and variability, *J. Climate*, 34, 949-965,  
749 <https://doi.org/10.1175/JCLI-D-20-0386.1>, 2021.
- 750
- 751 Bushuk, M., Msadek, R., Winton, M., Vecchi, G., Yang, X., Rosati, A., and Gudgel, R.:  
752 Regional Arctic sea–ice prediction: potential versus operational seasonal forecast skill. *Clim.*  
753 *Dyn.*, 52, 2721-2743, <https://doi.org/10.1007/s00382-018-4288-y>, 2019.
- 754
- 755 Bushuk, M., Winton, M., Haumann, F. A., Delworth, T., Lu, F., Zhang, Y., Jia, L., Zhang, L.,  
756 Cooke, W., Harrison, M., Hurlin, B., Johnson, N. C., Kapnick, S. B., McHugh, C., Murakami,  
757 H., Rosati, A., Tseng, K., Wittenberg, A. T., Yang, X., and Zeng, F.: Seasonal Prediction and  
758 Predictability of Regional Antarctic Sea Ice, *J. Climate*, 34, 6207-6233,  
759 <https://doi.org/10.1175/JCLI-D-20-0965.1>, 2021.
- 760
- 761 Carsey, F. D.: Microwave observation of the Weddell Polynya. *Mon. Wea. Rev.*, 108, 2032-  
762 2044, [https://doi.org/10.1175/1520-0493\(1980\)108<2032:MOOTWP>2.0.CO;2](https://doi.org/10.1175/1520-0493(1980)108<2032:MOOTWP>2.0.CO;2), 1980.
- 763
- 764 Cavalieri, D. J., Parkinson, C. L., and Vinnikov, K. Y.: 30-Year satellite record reveals  
765 contrasting Arctic and Antarctic decadal sea ice variability, *Geophys. Res. Lett.*, 30,  
766 <https://doi.org/10.1029/2003GL018031>, 2003.
- 767
- 768 Cheon, W. G., Park, Y. G., Toggweiler, J. R., and Lee, S. K.: The relationship of Weddell  
769 Polynya and open-ocean deep convection to the Southern Hemisphere westerlies, *J. Phys.*  
770 *Oceanogr.*, 44, 694-713, <https://doi.org/10.1175/JPO-D-13-0112.1>, 2014.

771  
772 Cheon, W. G., Lee, S. K., Gordon, A. L., Liu, Y., Cho, C. B., and Park, J. J.: Replicating the  
773 1970s' Weddell polynya using a coupled ocean-sea ice model with reanalysis surface flux fields,  
774 *Geophys. Res. Lett.*, 42, 5411-5418, <https://doi.org/10.1002/2015GL064364>, 2015.  
775  
776 Cheon, W. G., and Gordon, A. L.: Open-ocean polynyas and deep convection in the Southern  
777 Ocean, *Sci. Rep.*, 9, 1-9, <https://doi.org/10.1038/s41598-019-43466-2>, 2019.  
778  
779 Crosta, X., Etourneau, J., Orme, L.C. *et al.*: Multi-decadal trends in Antarctic sea-ice extent  
780 driven by ENSO–SAM over the last 2,000 years, *Nat. Geosci.*, 14, 156–160,  
781 <https://doi.org/10.1038/s41561-021-00697-1>, 2021.  
782  
783 de Lavergne, C., Palter, J. B., Galbraith, E. D., Bernardello, R., and Marinov, I.: Cessation of  
784 deep convection in the open Southern Ocean under anthropogenic climate change, *Nature*  
785 *Climate Change*, 4, 278-282, <https://doi.org/10.1038/nclimate2132>, 2014.  
786  
787 Delworth, T. L., Cooke, W. F., Adcroft, A., Bushuk, M., Chen, J.-H., Dunne, K. A., et al.:  
788 SPEAR: The next generation GFDL modeling system for seasonal to multidecadal prediction  
789 and projection, *J. Adv. Mod. Ear. Sys.*, 12, e2019MS001895,  
790 <https://doi.org/10.1029/2019MS001895>, 2020.  
791  
792 Eade, R., Smith, D., Scaife, A., Wallace, E., Dunstone, N., Hermanson, L., and Robinson, N.:  
793 Do seasonal-to-decadal climate predictions underestimate the predictability of the real world?  
794 *Geophys. Res. Lett.*, 41, 5620-5628, <https://doi.org/10.1002/2014GL061146>, 2014.  
795  
796 Eayrs, C., Li, X., Raphael, M. N., and Holland, D. M.: Rapid decline in Antarctic sea ice in  
797 recent years hints at future change, *Nature Geoscience*, 14, 460-464,  
798 <https://doi.org/10.1038/s41561-021-00768-3>, 2021.  
799  
800 Eyring, V., Bony, S., Meehl, G. A., Senior, C. A., Stevens, B., Stouffer, R. J., and Taylor, K.  
801 E.: Overview of the Coupled Model Intercomparison Project Phase 6 (CMIP6) experimental  
802 design and organization, *Geo. Mod. Dev.*, 9, 1937-1958, [https://doi.org/10.5194/gmd-9-1937-](https://doi.org/10.5194/gmd-9-1937-2016)  
803 [2016](https://doi.org/10.5194/gmd-9-1937-2016), 2016.  
804

805 Ferreira, D., Marshall, J., Bitz, C. M., Solomon, S., and Plumb, A.: Antarctic Ocean and sea  
806 ice response to ozone depletion: A two-time-scale problem, *J. Climate*, 28, 1206-1226,  
807 <https://doi.org/10.1175/JCLI-D-14-00313.1>, 2015.

808

809 Fogt, R. L., Sleinkofer, A. M., Raphael, M. N., and Handcock, M. S.: A regime shift in seasonal  
810 total Antarctic sea ice extent in the twentieth century, *Nature Climate Change*, 12, 54-62,  
811 <https://doi.org/10.1038/s41558-021-01254-9>, 2022.

812

813 Francis, D., Eayrs, C., Cuesta, J., and Holland, D.: Polar cyclones at the origin of the  
814 reoccurrence of the Maud Rise Polynya in austral winter 2017, *J. Geophys. Res. Atmos.*, 124,  
815 5251-5267, <https://doi.org/10.1029/2019JD030618>, 2019.

816

817 Francis, D., Mattingly, K. S., Temimi, M., Massom, R., and Heil, P.: On the crucial role of  
818 atmospheric rivers in the two major Weddell Polynya events in 1973 and 2017 in Antarctica,  
819 *Sci. Adv.*, 6, eabc2695, <https://doi.org/10.1126/sciadv.abc2695>, 2020.

820

821 Gagné, M. È., Gillett, N. P., and Fyfe, J. C.: Observed and simulated changes in Antarctic sea  
822 ice extent over the past 50 years, *Geophys. Res. Lett.*, 42, 90-95,  
823 <https://doi.org/10.1002/2014GL062231>, 2015.

824

825 Gong, D., and Wang, S.: Definition of Antarctic oscillation index, *Geophys. Res. Lett.*, 26,  
826 459-462, <https://doi.org/10.1029/1999GL900003>, 1999.

827

828 Good, S. A., Martin, M. J., and Rayner, N. A.: EN4: Quality controlled ocean temperature and  
829 salinity profiles and monthly objective analyses with uncertainty estimates, *J. Geophys. Res.*  
830 *Oce.*, 118, 6704– 6716, <https://doi.org/10.1002/2013JC009067>, 2013.

831

832 Goosse, H., and Fichefet, T.: Open-ocean convection and polynya formation in a large-scale  
833 ice-ocean model, *Tellus A* 53, 94-111, <https://doi.org/10.1034/j.1600-0870.2001.01061.x>,  
834 2001.

835

836 Goosse, H., and Zunz, V.: Decadal trends in the Antarctic sea ice extent ultimately controlled  
837 by ice–ocean feedback, *The Cryosphere* 8, 453-470, <https://doi.org/10.5194/tc-8-453-2014>,  
838 2014.

839  
840 Gordon, A. L.: Deep antarctic convection west of Maud Rise, *J. Phys. Oceanogr.*, 8, 600-612,  
841 [https://doi.org/10.1175/1520-0485\(1978\)008<0600:DACWOM>2.0.CO;2](https://doi.org/10.1175/1520-0485(1978)008<0600:DACWOM>2.0.CO;2), 1978.  
842  
843 Gordon, A. L., Visbeck, M., and Comiso, J. C.: A possible link between the Weddell Polynya  
844 and the Southern Annular Mode, *J. Climate*, 20, 2558-2571,  
845 <https://doi.org/10.1175/JCLI4046.1>, 2007.  
846  
847 Guemas, V., Doblas-Reyes, F. J., Mogensen, K., Keeley, S., and Tang, Y.: Ensemble of sea ice  
848 initial conditions for interannual climate predictions, *Clim. Dyn.*, 43, 2813-2829,  
849 <https://doi.org/10.1007/s00382-014-2095-7>, 2014.  
850  
851 Guemas, V., Chevallier, M., Déqué, M., Bellprat, O., and Doblas-Reyes, F.: Impact of sea ice  
852 initialization on sea ice and atmosphere prediction skill on seasonal timescales, *Geophys. Res.*  
853 *Lett.*, 43, 3889-3896, <https://doi.org/10.1002/2015GL066626>, 2016.  
854  
855 Hallberg, R.: Using a resolution function to regulate parameterizations of oceanic mesoscale  
856 eddy effects. *Ocean Modelling*, 72, 92-103, <https://doi.org/10.1016/j.ocemod.2013.08.007>  
857 2013.  
858  
859 Hellmer, H. H., Kauker, F., and Timmermann, R.: Weddell Sea anomalies: Excitation,  
860 propagation, and possible consequences, *Geophys. Res. Lett.*, 36, L12605,  
861 <https://doi.org/10.1029/2009GL038407>, 2009.  
862  
863 Henley, B. J., Gergis, J., Karoly, D. J., Power, S., Kennedy, J., and Folland, C. K.: A tripole  
864 index for the interdecadal Pacific oscillation, *Clim. Dyn.*, 45, 3077-3090,  
865 <https://doi.org/10.1007/s00382-015-2525-1>, 2015.  
866  
867 Hobbs, W. R., Massom, R., Stammerjohn, S., Reid, P., Williams, G., and Meier, W.: A review  
868 of recent changes in Southern Ocean sea ice, their drivers and forcings, *Global Planetary*  
869 *Change*, 143, 228-250, <https://doi.org/10.1016/j.gloplacha.2016.06.008>, 2016.  
870  
871 Holland, P. R., and Kwok, R.: Wind-driven trends in Antarctic sea-ice drift, *Nat. Geo.*, 5, 872-  
872 875, <https://doi.org/10.1038/ngeo1627>, 2012.

873  
874 Huang, B., Thorne, P. W., Banzon, V. F., Boyer, T., Chepurin, G., Lawrimore, J. H., Menne,  
875 M. J., Smith, T. M., Vose, R. S., and Zhang, H.: Extended Reconstructed Sea Surface  
876 Temperature, Version 5 (ERSSTv5): Upgrades, Validations, and Intercomparisons, *J. Climate*,  
877 30, 8179-8205, <https://doi.org/10.1175/JCLI-D-16-0836.1>, 2017.

878  
879 Killworth, P. D.: Deep convection in the world ocean, *Rev. Geophys.*, 21, 1-26,  
880 <https://doi.org/10.1029/RG021i001p00001>, 1983.

881  
882 Kobayashi, S., Ota, Y., Harada, Y., Ebata, A., Moriya, M., Onoda, H., *et al.*: The JRA-55  
883 reanalysis: general specifications and basic characteristics, *J. Meteorol. Soc. Japan. Ser. II*, 93,  
884 5-48, <https://doi.org/10.2151/jmsj.2015-001>, 2015.

885  
886 Kriegler, E., Bauer, N., Popp, A., Humpenöder, F., Leimbach, M., Strefler, J., *et al.*: Fossil-  
887 fueled development (SSP5): an energy and resource intensive scenario for the 21st century,  
888 *Global Env. Change*, 42, 297-315, <https://doi.org/10.1016/j.gloenvcha.2016.05.015>, 2017.

889  
890 Li, X., Holland, D. M., Gerber, E. P., and Yoo, C.: Impacts of the north and tropical Atlantic  
891 Ocean on the Antarctic Peninsula and sea ice, *Nature*, 505, 538-542,  
892 <https://doi.org/10.1038/nature12945>, 2014.

893  
894 Marchi, S., Fichefet, T., Goosse, H., Zunz, V., Tietsche, S., Day, J. J., and Hawkins, E.:  
895 Reemergence of Antarctic sea ice predictability and its link to deep ocean mixing in global  
896 climate models, *Clim. Dyn.*, 52, 2775-2797, <https://doi.org/10.1007/s00382-018-4292-2>, 2019.

897  
898 Martinson, D. G., Killworth, P. D., and Gordon, A. L.: A convective model for the Weddell  
899 Polynya, *J. Phys. Oceanogr.*, 11, 466-488, [https://doi.org/10.1175/1520-0485\(1981\)011<0466:ACMFTW>2.0.CO;2](https://doi.org/10.1175/1520-0485(1981)011<0466:ACMFTW>2.0.CO;2), 1981.

900  
901  
902 Meehl, G. A., Arblaster, J. M., Bitz, C. M., Chung, C. T., and Teng, H. Antarctic sea-ice  
903 expansion between 2000 and 2014 driven by tropical Pacific decadal climate variability, *Nat.*  
904 *Geo.*, 9, 590-595, <https://doi.org/10.1038/ngeo2751>, 2016.

905

906 Meehl, G. A., Arblaster, J. M., Chung, C. T., Holland, M. M., DuVivier, A., Thompson, L., *et*  
907 *al.*: Sustained ocean changes contributed to sudden Antarctic sea ice retreat in late 2016, *Nat.*  
908 *Comm.*, 10, 1-9, <https://doi.org/10.1038/s41467-018-07865-9>, 2019.

909

910 Meier, W. N., Gallaher, D., Campbell, G. G.: New estimates of Arctic and Antarctic sea ice  
911 extent during September 1964 from recovered Nimbus I satellite imagery, *The Cryosphere*, 7,  
912 699-705, <https://doi.org/10.5194/tc-7-699-2013>, 2013.

913

914 Meier, W. N., F. Fetterer, A. K. Windnagel, and J. S. Stewart.: NOAA/NSIDC Climate Data  
915 Record of Passive Microwave Sea Ice Concentration, Version 4, Boulder, Colorado USA,  
916 NSIDC: National Snow and Ice Data Center, <https://doi.org/10.7265/efmz-2t65>, 2021.

917

918 Morales Maqueda, M. A., Willmott, A. J., and Biggs, N. R. T.: Polynya dynamics: A review  
919 of observations and modeling, *Rev. Geophys.*, 42, <https://doi.org/10.1029/2002RG000116>,  
920 2004.

921

922 Morioka, Y., and Behera, S. K.: Remote and local processes controlling decadal sea ice  
923 variability in the Weddell Sea, *J. Geophys. Res. Oce.*, 126, e2020JC017036,  
924 <https://doi.org/10.1029/2020JC017036>, 2021.

925

926 Morioka, Y., Iovino, D., Masina, S., and Behera, S. K.: Role of sea-ice initialization in climate  
927 predictability over the Weddell Sea, *Sci. Rep.*, 9, 1-11, [https://doi.org/10.1038/s41598-019-](https://doi.org/10.1038/s41598-019-39421-w)  
928 [39421-w](https://doi.org/10.1038/s41598-019-39421-w), 2019.

929

930 Morioka, Y., Iovino, D., Cipollone, A., Masina, S., and Behera, S. K.: Summertime sea-ice  
931 prediction in the Weddell Sea improved by sea-ice thickness initialization, *Sci. Rep.*, 11, 1-13,  
932 <https://doi.org/10.1038/s41598-021-91042-4>, 2021.

933

934 Morioka, Y., Iovino, D., Cipollone, A., Masina, S., and Behera, S. K.: Decadal Sea Ice  
935 Prediction in the West Antarctic Seas with Ocean and Sea Ice Initializations, *Comm. Earth*  
936 *Env.*, 3, 1-10, <https://doi.org/10.1038/s43247-022-00529-z>, 2022.

937

938 Murphy, E. J., Clarke, A., Abram, N. J., and Turner, J.: Variability of sea-ice in the northern  
939 Weddell Sea during the 20th century, *J. Geophys. Res. Oce.*, 119, 4549–4572,  
940 <https://doi.org/10.1002/2013JC009511>, 2014.

941

942 Orsi, A. H., Johnson, G. C., and Bullister, J. L.: Circulation, mixing, and production of  
943 Antarctic Bottom Water, *Prog. Oceanogr.*, 43, 55-109, [https://doi.org/10.1016/S0079-  
944 6611\(99\)00004-X](https://doi.org/10.1016/S0079-6611(99)00004-X), 1999.

945

946 Parkinson, C. L.: A 40-y record reveals gradual Antarctic sea ice increases followed by  
947 decreases at rates far exceeding the rates seen in the Arctic, *Proc. Nat. Aca. Sci.*, 116, 14414-  
948 14423, <https://doi.org/10.1073/pnas.1906556116>, 2019.

949

950 Polvani, L. M., and Smith, K. L.: Can natural variability explain observed Antarctic sea ice  
951 trends? New modeling evidence from CMIP5, *Geophys. Res. Lett.*, 40, 3195-3199,  
952 <https://doi.org/10.1002/grl.50578>, 2013.

953

954 Power, S., Casey, T., Folland, C., Colman, A., and Mehta, V.: Inter-decadal modulation of the  
955 impact of ENSO on Australia, *Clim. Dyn.*, 15, 319-324,  
956 <https://doi.org/10.1007/s003820050284>, 1999.

957

958 Rayner, N. A., Parker, D. E., Horton, E. B., Folland, C. K., Alexander, L. V., Rowell, D. P.,  
959 Kent, E. C., and Kaplan, A.: Global analyses of sea surface temperature, sea ice, and night  
960 marine air temperature since the late nineteenth century, *J. Geophys. Res.*, 108, 4407,  
961 <https://doi.org/10.1029/2002JD002670>, 2003.

962

963 Riahi, K., Van Vuuren, D. P., Kriegler, E., Edmonds, J., O’neill, B. C., Fujimori, S., et al.: The  
964 shared socioeconomic pathways and their energy, land use, and greenhouse gas emissions  
965 implications: an overview, *Global Env. Change*, 42, 153-168,  
966 <https://doi.org/10.1016/j.gloenvcha.2016.05.009>, 2017.

967

968 Roach, L. A., Dörr, J., Holmes, C. R., Massonnet, F., Blockley, E. W., Notz, D., et al.: Antarctic  
969 sea ice area in CMIP6, *Geophys. Res. Lett.*, 47, e2019GL086729,  
970 <https://doi.org/10.1029/2019GL086729>, 2020.

971

972 Scaife, A. A., and Smith, D.: A signal-to-noise paradox in climate science. *npj Clim. Atmos.*  
973 *Sci.*, 1, 28, <https://doi.org/10.1038/s41612-018-0038-4>, 2018.

974

975 Schlosser, E., Haumann, F. A., and Raphael, M. N.: Atmospheric influences on the anomalous  
976 2016 Antarctic sea ice decay, *The Cryosphere*, 12, 1103-1119, [https://doi.org/10.5194/tc-12-](https://doi.org/10.5194/tc-12-1103-2018)  
977 [1103-2018](https://doi.org/10.5194/tc-12-1103-2018), 2018.

978

979 Simpkins, G.: Record low Antarctic sea ice extent. *Nat Rev Earth Environ*, 4, 296.  
980 <https://doi.org/10.1038/s43017-023-00433-w>, 2023.

981

982 Stuecker, M. F., Bitz, C. M., and Armour, K. C.: Conditions leading to the unprecedented low  
983 Antarctic sea ice extent during the 2016 austral spring season, *Geophys. Res. Lett.*, 44, 9008-  
984 9019, <https://doi.org/10.1002/2017GL074691>, 2017.

985

986 Sun, S., and Eisenman, I.: Observed Antarctic sea ice expansion reproduced in a climate model  
987 after correcting biases in sea ice drift velocity, *Nat. Comm.*, 12, 1-6,  
988 <https://doi.org/10.1038/s41467-021-21412-z>, 2021.

989

990 Titchner, H. A., and Rayner, N. A.: The Met Office Hadley Centre sea ice and sea surface  
991 temperature data set, version 2: 1. Sea ice concentrations, *J. Geophys. Res. Atmos.*, 119, 2864-  
992 2889, <https://doi.org/10.1002/2013JD020316>, 2014.

993

994 Thompson, D. W., and Wallace, J. M.: Annular modes in the extratropical circulation. Part I:  
995 Month-to-month variability, *J. Climate*, 13, 1000-1016, [https://doi.org/10.1175/1520-](https://doi.org/10.1175/1520-0442(2000)013<1000:AMITEC>2.0.CO;2)  
996 [0442\(2000\)013<1000:AMITEC>2.0.CO;2](https://doi.org/10.1175/1520-0442(2000)013<1000:AMITEC>2.0.CO;2), 2000.

997

998 Turner, J., Hosking, J. S., Marshall, G. J., Phillips, T., and Bracegirdle, T. J.: Antarctic sea ice  
999 increase consistent with intrinsic variability of the Amundsen Sea Low, *Clim. Dyn.*, 46, 2391-  
1000 2402, <https://doi.org/10.1007/s00382-015-2708-9>, 2016.

1001

1002 Turner, J., Phillips, T., Marshall, G. J., Hosking, J. S., Pope, J. O., Bracegirdle, T. J., and Deb,  
1003 P.: Unprecedented springtime retreat of Antarctic sea ice in 2016, *Geophys. Res. Lett.*, 44,  
1004 6868-6875, <https://doi.org/10.1002/2017GL073656>, 2017.

1005

1006 Turner, J., Guarino, M. V., Arnatt, J., Jena, B., Marshall, G. J., Phillips, T., et al.: Recent  
1007 decrease of summer sea ice in the Weddell Sea, Antarctica, *Geophys. Res. Lett.*, 47,  
1008 e2020GL087127, <https://doi.org/10.1029/2020GL087127>, 2020.  
1009  
1010 Venegas, S. A., and Drinkwater, M. R.: Sea ice, atmosphere and upper ocean variability in the  
1011 Weddell Sea, Antarctica, *J. Geophys. Res.*, 106, 16747–16765,  
1012 <https://doi.org/10.1029/2000JC000594>, 2001.  
1013  
1014 Wang, G., Hendon, H. H., Arblaster, J. M., Lim, E. P., Abhik, S., and Rensch, P.: Compounding  
1015 tropical and stratospheric forcing of the record low Antarctic sea-ice in 2016, *Nat. Comm.*, 10,  
1016 1-9, <https://doi.org/10.1038/s41467-018-07689-7>, 2019.  
1017  
1018 Yang, C. Y., Liu, J., Hu, Y., Horton, R. M., Chen, L., and Cheng, X.: Assessment of Arctic  
1019 and Antarctic sea ice predictability in CMIP5 decadal hindcasts, *The Cryosphere*, 10, 2429-  
1020 2452, <https://doi.org/10.5194/tc-10-2429-2016>, 2016.  
1021  
1022 Yang, J., Xiao, C., Liu, J., Li, S., and Qin, D.: Variability of Antarctic sea ice extent over the  
1023 past 200 years, *Sci. Bull.*, 66, 2394-2404, <https://doi.org/10.1016/j.scib.2021.07.028>, 2021.  
1024  
1025 Yang, X., Delworth, T. L., Zeng, F., Zhang, L., Cooke, W. F., Harrison, M. J., et al.: On the  
1026 development of GFDL's decadal prediction system: Initialization approaches and retrospective  
1027 forecast assessment, *J. Adv. Mod. Earth Sys.*, 13, e2021MS002529,  
1028 <https://doi.org/10.1029/2021MS002529>, 2021.  
1029  
1030 Yuan, N., Ding, M., Ludescher, and J., Bunde, A.: Increase of the Antarctic Sea Ice Extent is  
1031 highly significant only in the Ross Sea. *Sci, Rep.*, 7, 1-8, <https://doi.org/10.1038/srep41096>,  
1032 2017.  
1033  
1034 Yuan, X., and Martinson, D. G.: Antarctic sea ice extent variability and its global connectivity,  
1035 *J. Climate*, 13, 1697-1717, [https://doi.org/10.1175/1520-  
1036 0442\(2000\)013<1697:ASIEVA>2.0.CO;2](https://doi.org/10.1175/1520-0442(2000)013<1697:ASIEVA>2.0.CO;2), 2000.  
1037

1038 Zhang, L., Delworth, T. L., Cooke, W., and Yang, X.: Natural variability of Southern Ocean  
1039 convection as a driver of observed climate trends, *Nat. Clim. Change*, 9, 59-65,  
1040 <https://doi.org/10.1038/s41558-018-0350-3>, 2019.

1041

1042 Zhang, L., Delworth, T. L., Cooke, W., Goosse, H., Bushuk, M., Morioka, Y., and Yang, X:  
1043 The dependence of internal multidecadal variability in the Southern Ocean on the ocean  
1044 background mean state, *J. Climate*, 34, 1061-1080, <https://doi.org/10.1175/JCLI-D-20-0049.1>,  
1045 2021.

1046

1047 Zhang, L., Delworth, T. L., Kapnick, S., He, J., Cooke, W., Wittenberg, A. T., Johnson, N. C.,  
1048 Rosati, A., Yang, X., Lu, F., Bushuk, M., McHugh, C., Murakami, H., Zeng, F., Jia, L., Tseng,  
1049 K., and Morioka, Y.: Roles of Meridional Overturning in Subpolar Southern Ocean SST  
1050 Trends: Insights from Ensemble Simulations, *J. Climate*, 35, 1577-1596,  
1051 <https://doi.org/10.1175/JCLI-D-21-0466.1>, 2022a.

1052

1053 Zhang, L., Delworth, T. L., Yang, X., Zeng, F., Lu, F., Morioka, Y., and Bushuk, M.: The  
1054 relative role of the subsurface Southern Ocean in driving negative Antarctic Sea ice extent  
1055 anomalies in 2016–2021, *Comm. Earth Env.*, 3, 1-9, [https://doi.org/10.1038/s43247-022-](https://doi.org/10.1038/s43247-022-00624-1)  
1056 [00624-1](https://doi.org/10.1038/s43247-022-00624-1), 2022b.

1057

1058

1059 Zhao, M., Golaz, J.-C., Held, I. M., Guo, H., Balaji, V., Benson, R., et al.: The GFDL global  
1060 atmosphere and land model AM4.0/LM4.0: 1. Simulation characteristics with prescribed SSTs,  
1061 *J. Adv. Mod. Earth Sys.*, 10, 691–734, <https://doi.org/10.1002/2017MS001208>, 2018.

1062

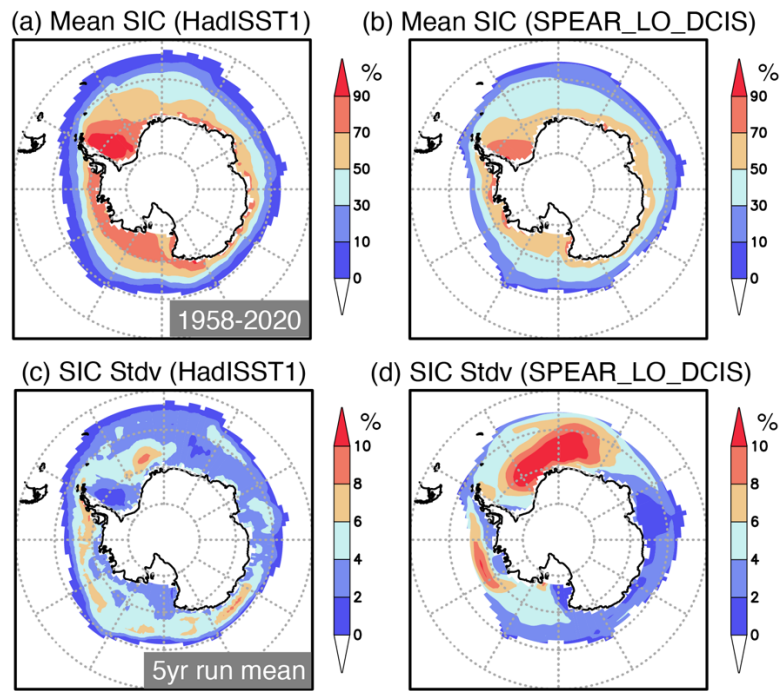
1063 Zhao, M., Golaz, J.-C., Held, I. M., Guo, H., Balaji, V., Benson, R., et al.: The GFDL global  
1064 atmosphere and land model AM4.0/LM4.0: 2. Model description, sensitivity studies, and  
1065 tuning strategies, *J. Adv. Mod. Earth Sys.*, 10, 735–769,  
1066 <https://doi.org/10.1002/2017MS001209>, 2018.

1067

1068 Zunz, V., Goosse, H., and Dubinkina, S.: Impact of the initialisation on the predictability of  
1069 the Southern Ocean sea ice at interannual to multi-decadal timescales, *Clim. Dyn.*, 44, 2267-  
1070 2286, <https://doi.org/10.1007/s00382-014-2344-9>, 2015.

1071

1072 **Figures**



1073

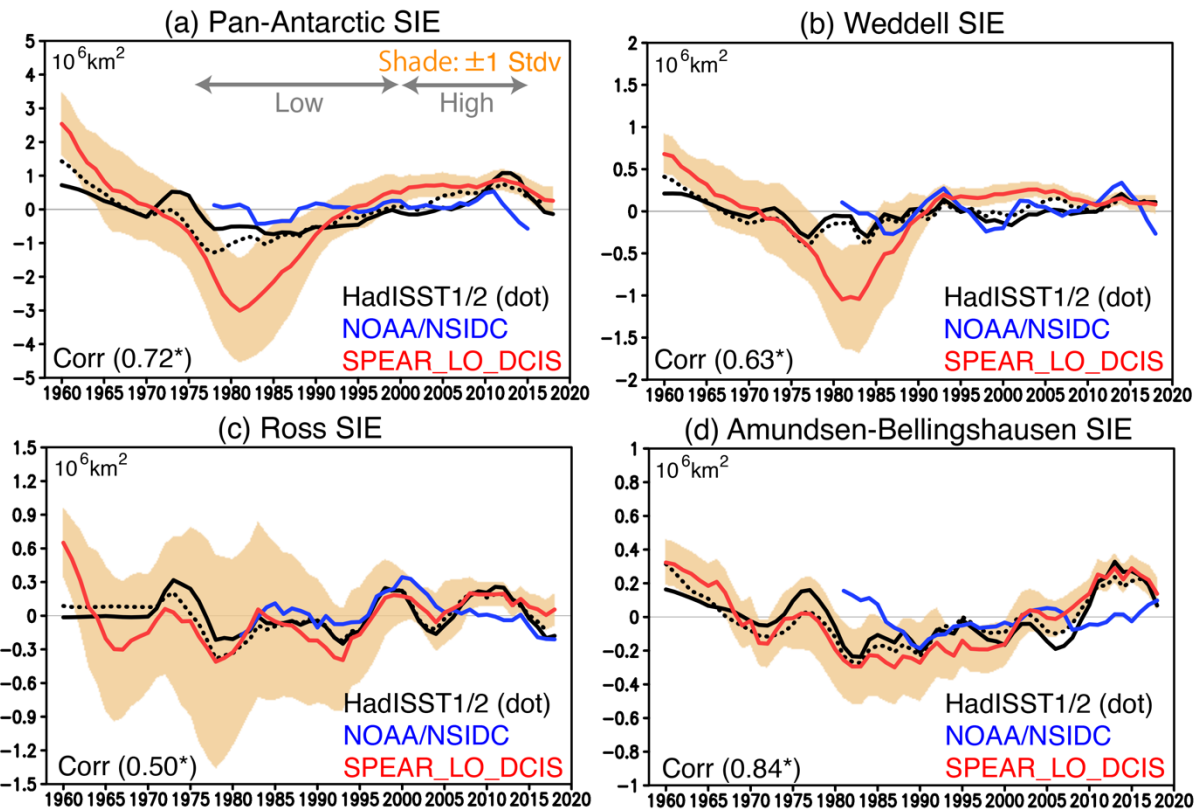
1074 **Figure 1 (a)** Annual mean sea ice concentration (SIC in %) observed during 1958-2020. **(b)**

1075 Same as in **(a)**, but for the simulated SIC from the SPEAR\_LO\_DCIS. **(c)** Standard deviation

1076 of 5-yr running mean SIC (in %) observed during 1958-2020. **(d)** Same as in **(c)**, but for the

1077 simulated SIC from the SPEAR\_LO\_DCIS.

1078



1079

1080

1081

1082

1083

1084

1085

1086

1087

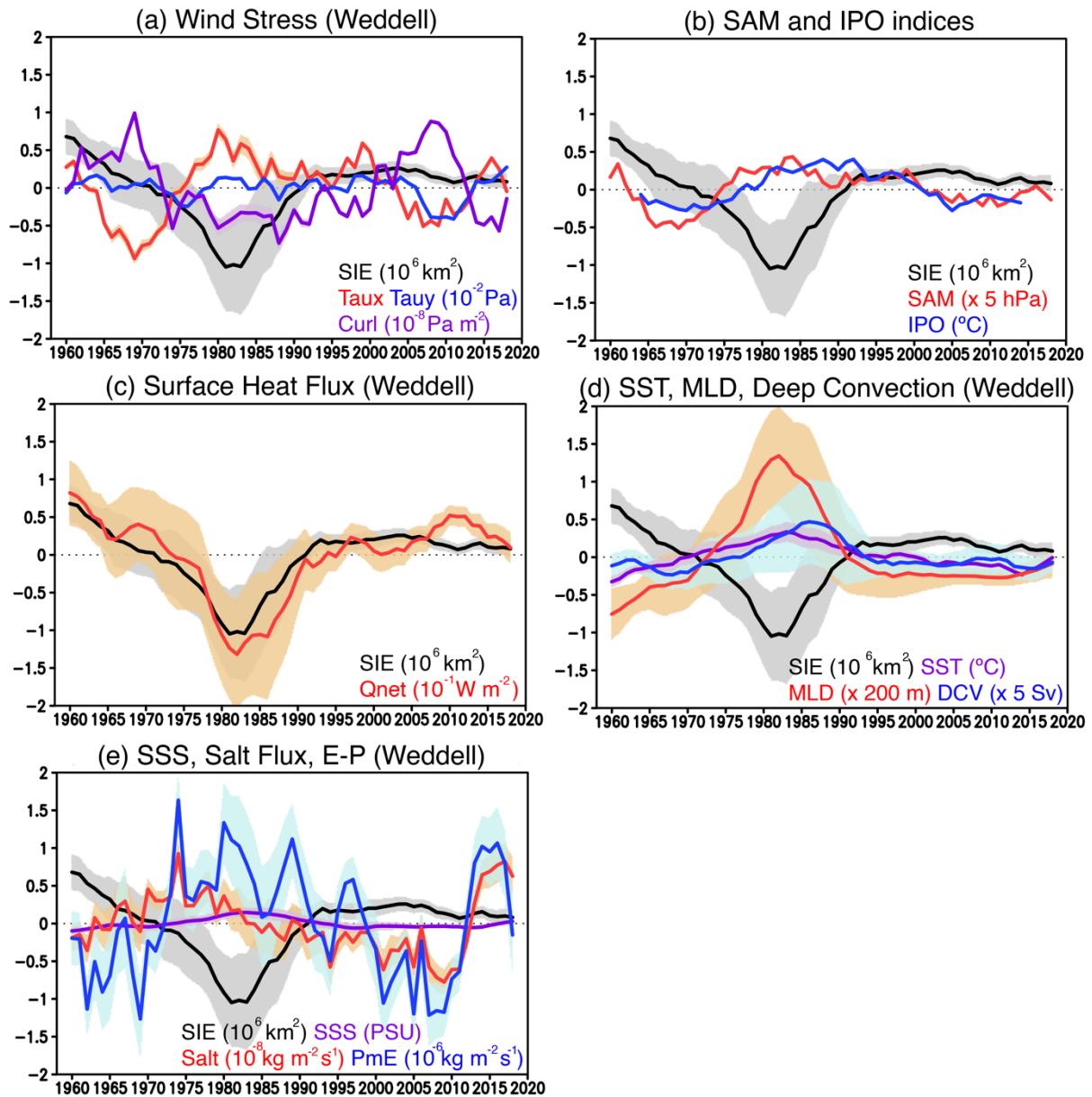
1088

1089

1090

1091

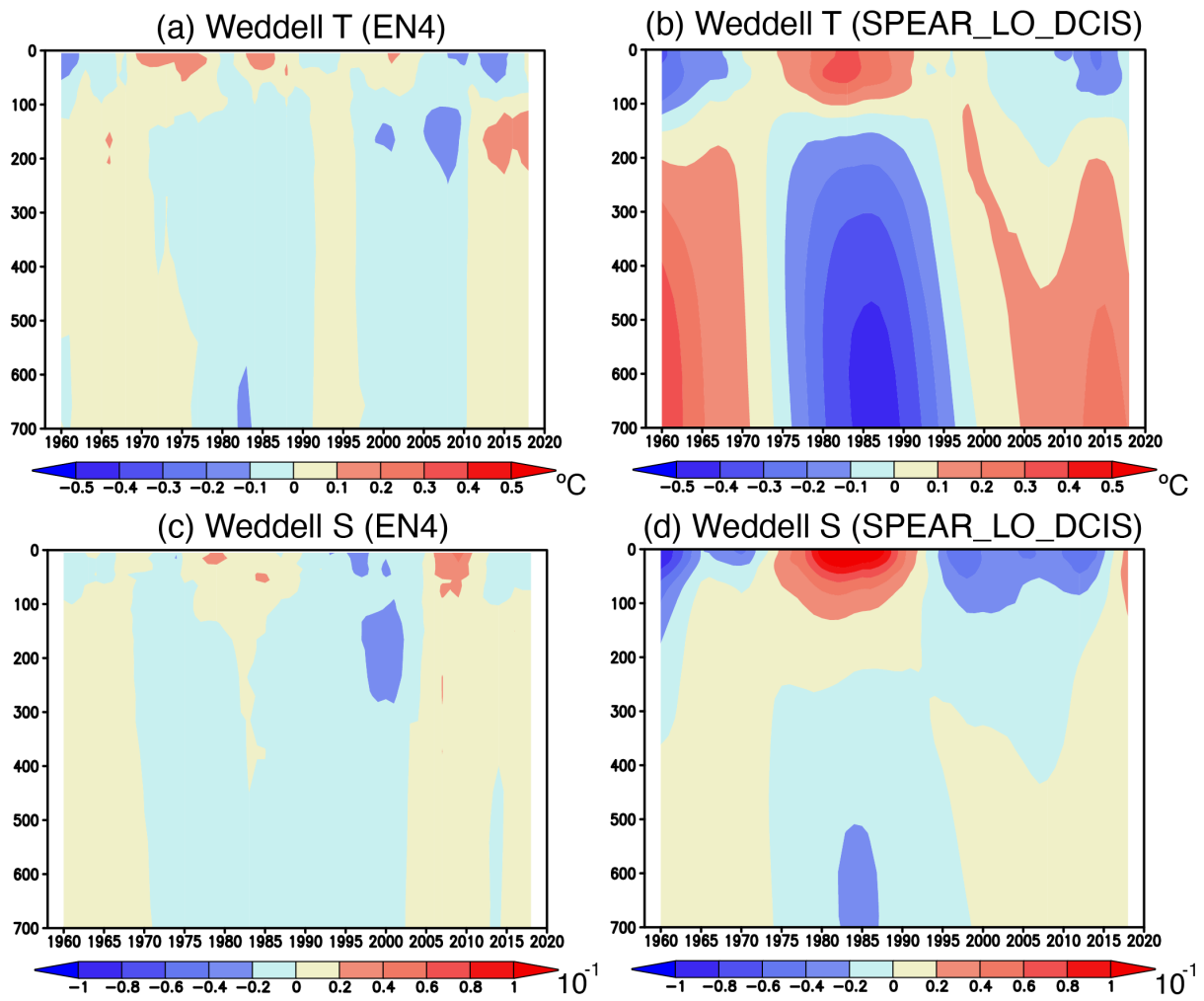
**Figure 2** (a) Time series of 5-yr running mean sea ice extent (SIE in  $10^6 \text{ km}^2$ ) anomalies in the pan-Antarctic region during 1958-2020. Observations from HadISST1 (black solid), HadISST2 (black dotted) and the NOAA/NSIDC (blue) are shown, whereas the SPEAR\_LO\_DCIS is shown with a red line. Orange shades indicate one and minus one standard deviations of the SIE anomalies simulated from 30 ensemble members of SPEAR\_LO\_DCIS. Gray arrows correspond to a low sea ice period (late 1970s-1990s) and a high sea ice period (2000s-early 2010s). Correlation coefficient between HadISST1 and the SPEAR\_LO\_DCIS is shown in the bottom left where the asterisk indicates the statistically significant correlation at 90 % confidence level using Student's *t*-test. (b-d) Same as in (a), but for the SIE anomalies in the Weddell Sea ( $60^\circ\text{-}0^\circ\text{W}$ ), Ross Sea ( $180^\circ\text{-}120^\circ\text{W}$ ), and Amundsen-Bellingshausen Sea ( $120^\circ\text{-}60^\circ\text{W}$ ), respectively.



1092

1093 **Figure 3 (a)** Time series of 5-yr running mean SIE (black line in  $10^6 \text{ km}^2$ ), zonal (Taux; red in  
 1094  $10^{-2} \text{ Pa}$ ) and meridional (Tauy; blue in  $10^{-2} \text{ Pa}$ ) wind stress, and wind stress curl (Curl; purple  
 1095 in  $10^{-8} \text{ Pa m}^{-2}$ ) anomalies averaged in the Weddell Sea ( $60^\circ\text{W}$ - $0^\circ$ , south of  $55^\circ\text{S}$ ) during 1958-  
 1096 2020. Shades indicate one and minus one standard deviations of the anomalies from 30  
 1097 ensemble members of the SPEAR\_LO\_DCIS. Positive wind stress curl anomalies correspond  
 1098 to downwelling anomalies in the ocean. **(b)** Same as in **(a)**, but for the 5-yr running mean SAM  
 1099 index (red in 5 hPa) and 13-yr running mean IPO index (blue in  $^\circ\text{C}$ ). **(c)** Same as in **(a)**, but for  
 1100 the SIE (black in  $10^6 \text{ km}^2$ ) and the net surface heat flux (Qnet; red in  $10^{-1} \text{ W m}^{-2}$ ) anomalies.  
 1101 Positive surface heat flux anomalies correspond to more heat going into the ocean. **(d)** Same  
 1102 as in **(a)**, but for the SIE (black in  $10^6 \text{ km}^2$ ), sea surface temperature (SST; purple in  $^\circ\text{C}$ ), mixed-  
 1103 layer depth (MLD; red in 200 m), and deep convection (DCV; blue in 5 Sv) anomalies. **(e)**

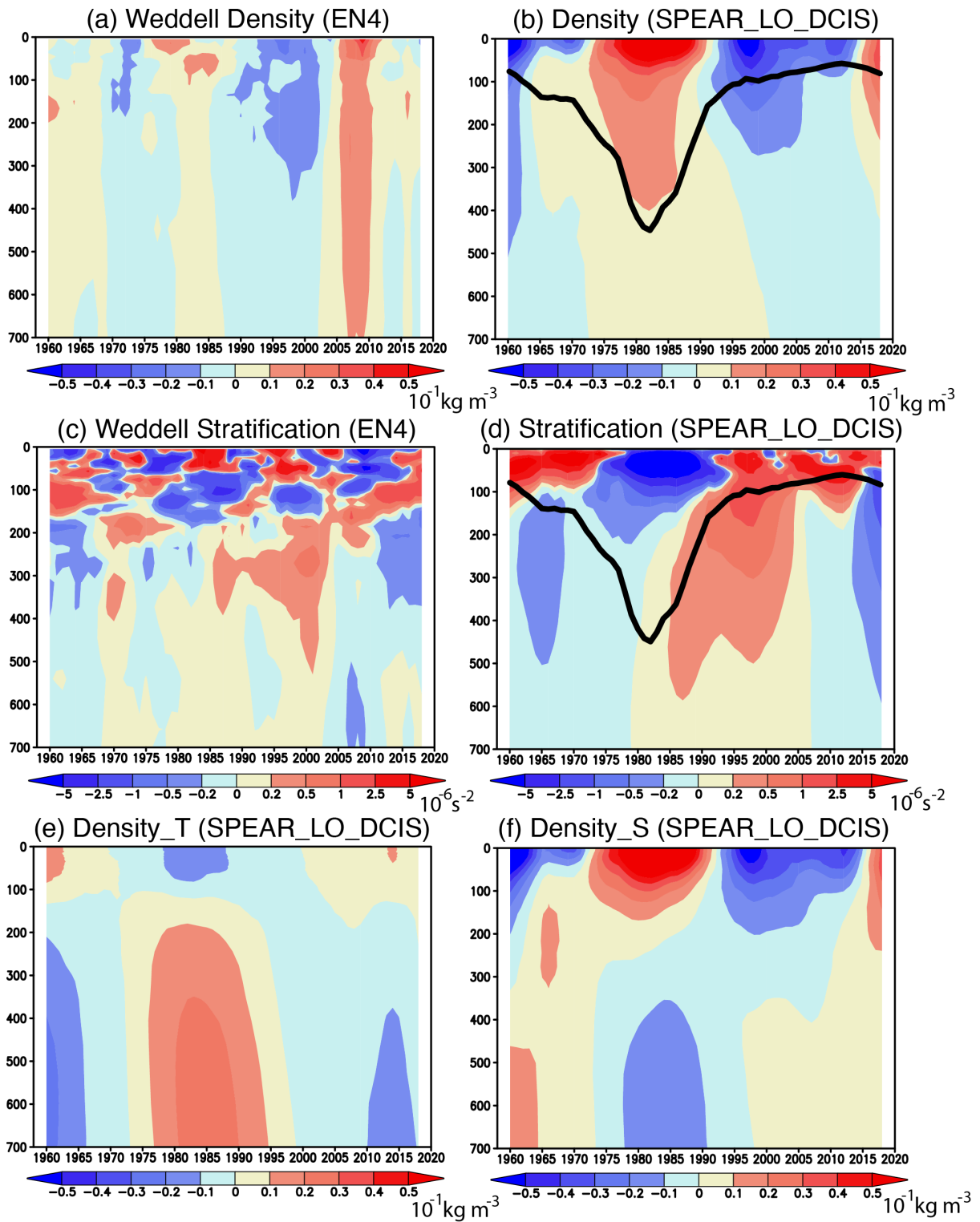
1104 Same as in **(a)**, but for the SIE (black in  $10^6 \text{ km}^2$ ), sea surface salinity (SSS; purple in PSU),  
1105 salt flux (Salt; red in  $10^{-8} \text{ kg m}^{-2} \text{ s}^{-1}$ ), and precipitation minus evaporation (PmE; blue in  $10^{-6}$   
1106  $\text{kg m}^{-2} \text{ s}^{-1}$ ) anomalies. Positive salt flux anomalies correspond to anomalous salt going into the  
1107 ocean at the surface associated with sea ice formation, whereas the positive PmE anomalies  
1108 mean more freshwater going into the ocean.  
1109



1110

1111 **Figure 4 (a)** Temporal evolution of 5-yr running mean ocean temperature (in  $^{\circ}\text{C}$ ) anomalies  
 1112 averaged in the Weddell Sea as a function of depth (in m). **(b)** Same as in **(a)**, but for the ocean  
 1113 temperature anomalies simulated from the SPEAR\_LO\_DCIS. **(c)** Temporal evolution of  
 1114 ocean salinity (in  $10^{-1}$  PSU) anomalies averaged in the Weddell Sea as a function of depth (in  
 1115 m). **(d)** Same as in **(a)**, but for the ocean salinity anomalies simulated from the  
 1116 SPEAR\_LO\_DCIS.

1117



1118

1119

1120

1121

1122

1123

1124

**Figure 5** (a) Temporal evolution of 5-yr running mean ocean density anomalies (in  $10^{-1} \text{ kg m}^{-3}$ ) averaged in the Weddell Sea from the EN4 as a function of depth (in m). (b) Same as in (a), but for the SPEAR\_LO\_DCIS. A black line indicates a mixed-layer depth at which the ocean density increases by  $0.03 \text{ kg m}^{-3}$  from the one at the ocean surface. (c) Same as in (a), but for the ocean stratification (squared Brunt-Väisälä frequency in  $10^{-6} \text{ s}^{-2}$ ) anomalies. Positive stratification anomalies indicate a higher stability of sea water. (d) Same as in (c), but for the

1125 SPEAR\_LO\_DCIS. A black line indicates a mixed-layer depth at which the ocean density  
1126 increases by  $0.03 \text{ kg m}^{-3}$  from the one at the ocean surface. **(e)** Same as in **(b)**, but for the ocean  
1127 density anomalies (in  $10^{-1} \text{ kg m}^{-3}$ ) driven by the ocean temperature anomalies independent of  
1128 the ocean salinity anomalies. **(f)** Same as in **(b)**, but for the ocean density anomalies (in  $10^{-1} \text{ kg}$   
1129  $\text{m}^{-3}$ ) driven by the ocean salinity anomalies independent of the ocean temperature anomalies.  
1130

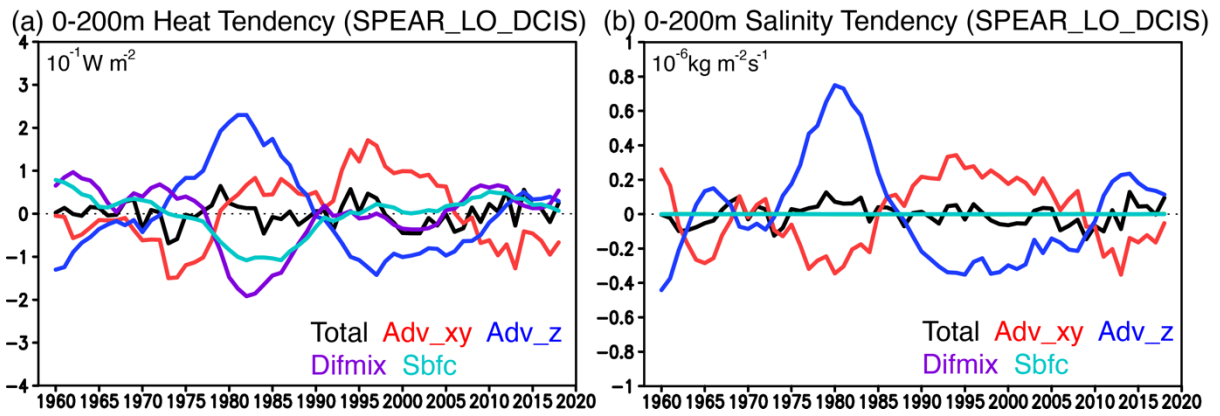
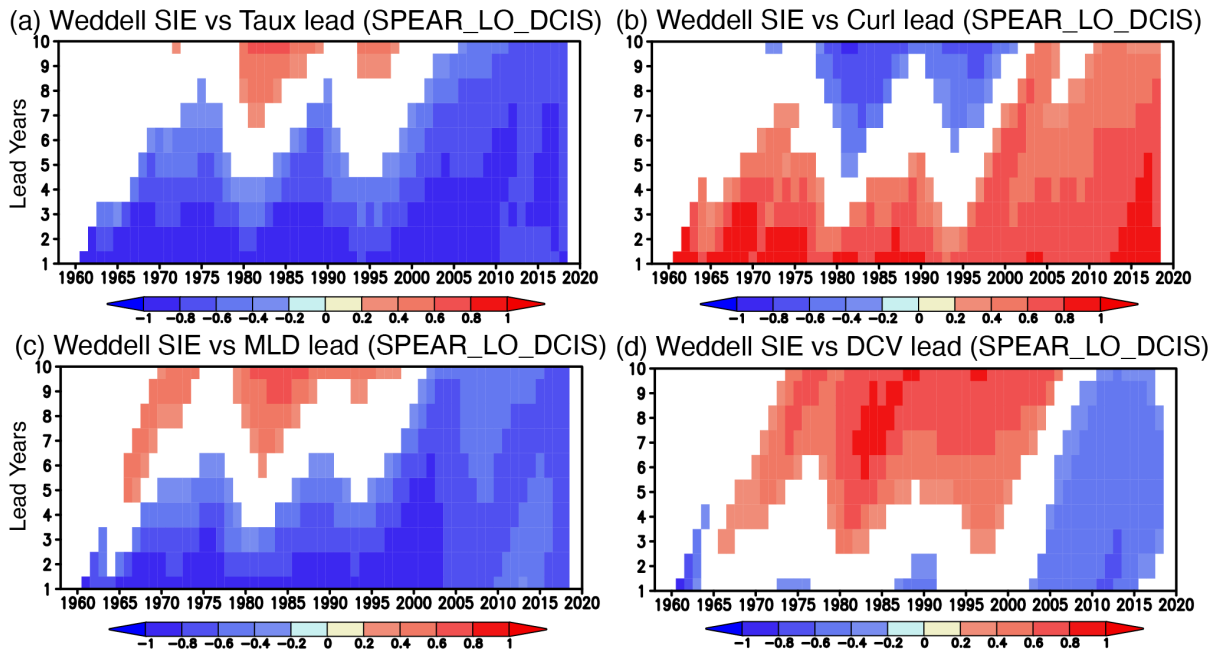


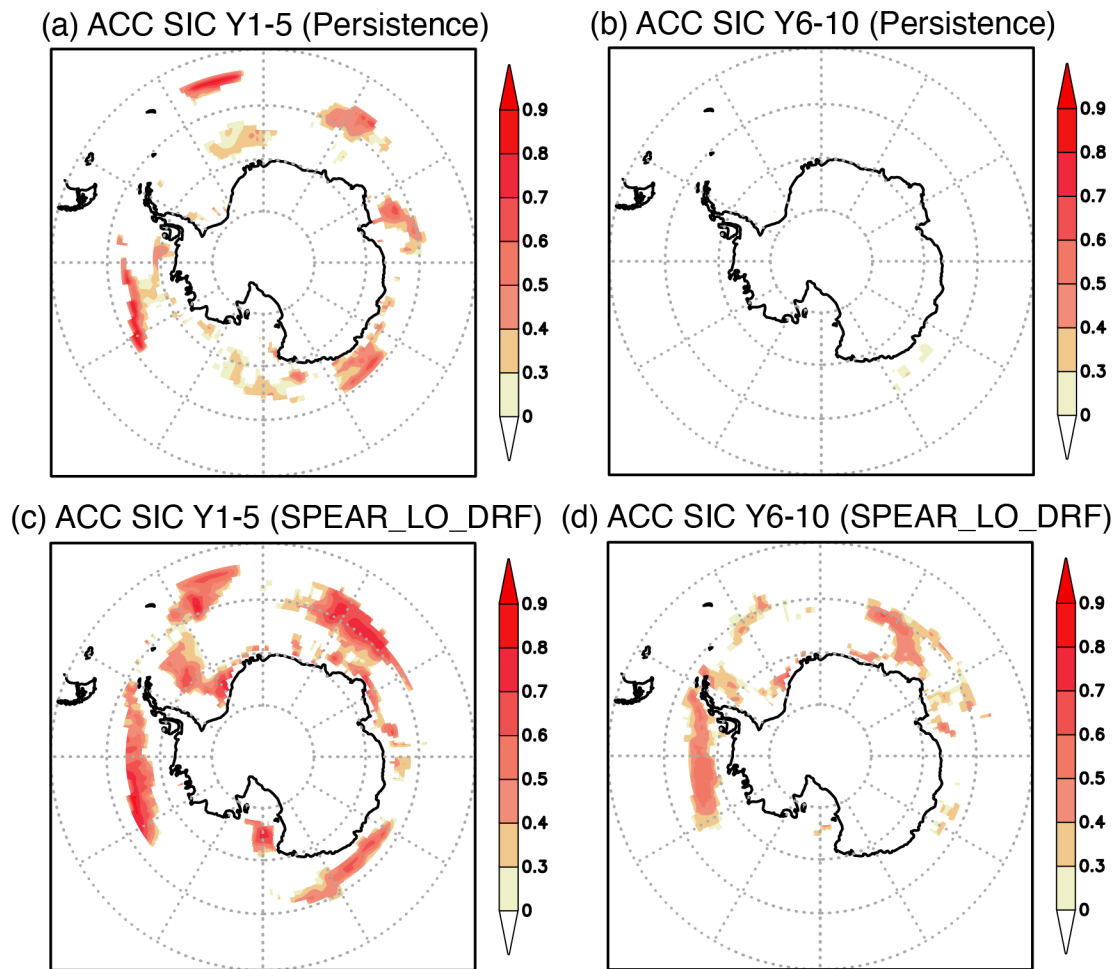
**Figure 6 (a)** Time series of 5-yr running mean ocean heat tendency (in  $10^{-1} \text{ W m}^{-2}$ ) anomalies in the upper 200 m of the Weddell Sea from the SPEAR\_LO\_DCIS. Total ocean heat tendency (Total; black), horizontal advection (Adv\_xy; red), vertical advection (Adv\_z; blue), mesoscale diffusion and diapycnal mixing (Difmix; purple), and surface boundary forcing (Sbfc; light blue) anomalies are shown, respectively. **(b)** Same as in **(a)**, but for the salinity tendency (in  $10^{-6} \text{ kg m}^{-2} \text{ s}^{-1}$ ) anomalies.



1139

1140 **Figure 7 (a)** Temporal evolution of inter-member correlation between the 5-yr running mean  
 1141 SIE anomalies and the 5-yr running mean zonal wind stress (Taux) averaged in the Weddell  
 1142 Sea from 30 ensemble members of the SPEAR\_LO\_DCIS as a function of lead years (y-axis).  
 1143 Positive lead years mean that the Taux anomalies lead the SIE anomalies by the number of  
 1144 years. Correlation coefficients that are statistically significant at 90 % using Student's *t*-test are  
 1145 shown in color. **(b)** Same as in **(a)**, but for the inter-member correlation between the SIE  
 1146 anomalies and the wind stress curl (Curl) anomalies. **(c)** Same as in **(a)**, but for the inter-  
 1147 member correlation between the SIE anomalies and the mixed-layer depth (MLD) anomalies.  
 1148 **(d)** Same as in **(a)**, but for the inter-member correlation between the SIE anomalies and the  
 1149 deep convection (DCV) anomalies.

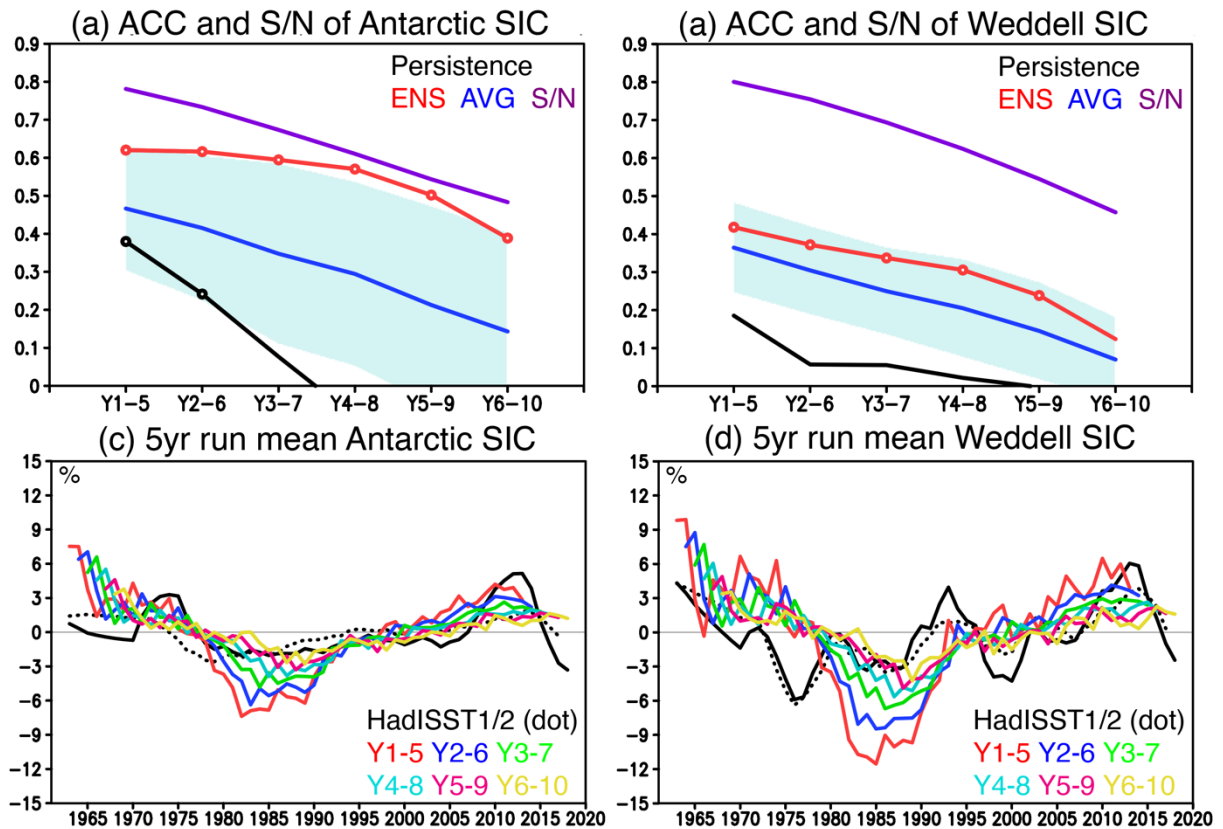
1150



1151

1152 **Figure 8** (a) Anomaly correlation (ACC) of the SIC anomalies from the persistence prediction  
 1153 at a lead time of 1-5 years. Positive ACCs that are statistically significant at 90 % using the  
 1154 Student's *t*-test are colored. (b) Same as in (a), but for the ACC from the persistence prediction  
 1155 at a lead time of 6-10 years. (c) Same as in (a), but for the ACC between the observed SIC  
 1156 anomalies and the ensemble mean SIC anomalies predicted at a lead time of 1-5 years in the  
 1157 SPEAR\_LO\_DRF. (d) Same as in (c), but for the ACCs of the ensemble mean SIC anomalies  
 1158 predicted at a lead time of 6-10 years in the SPEAR\_LO\_DRF.

1159



1160

1161

1162

1163

1164

1165

1166

1167

1168

1169

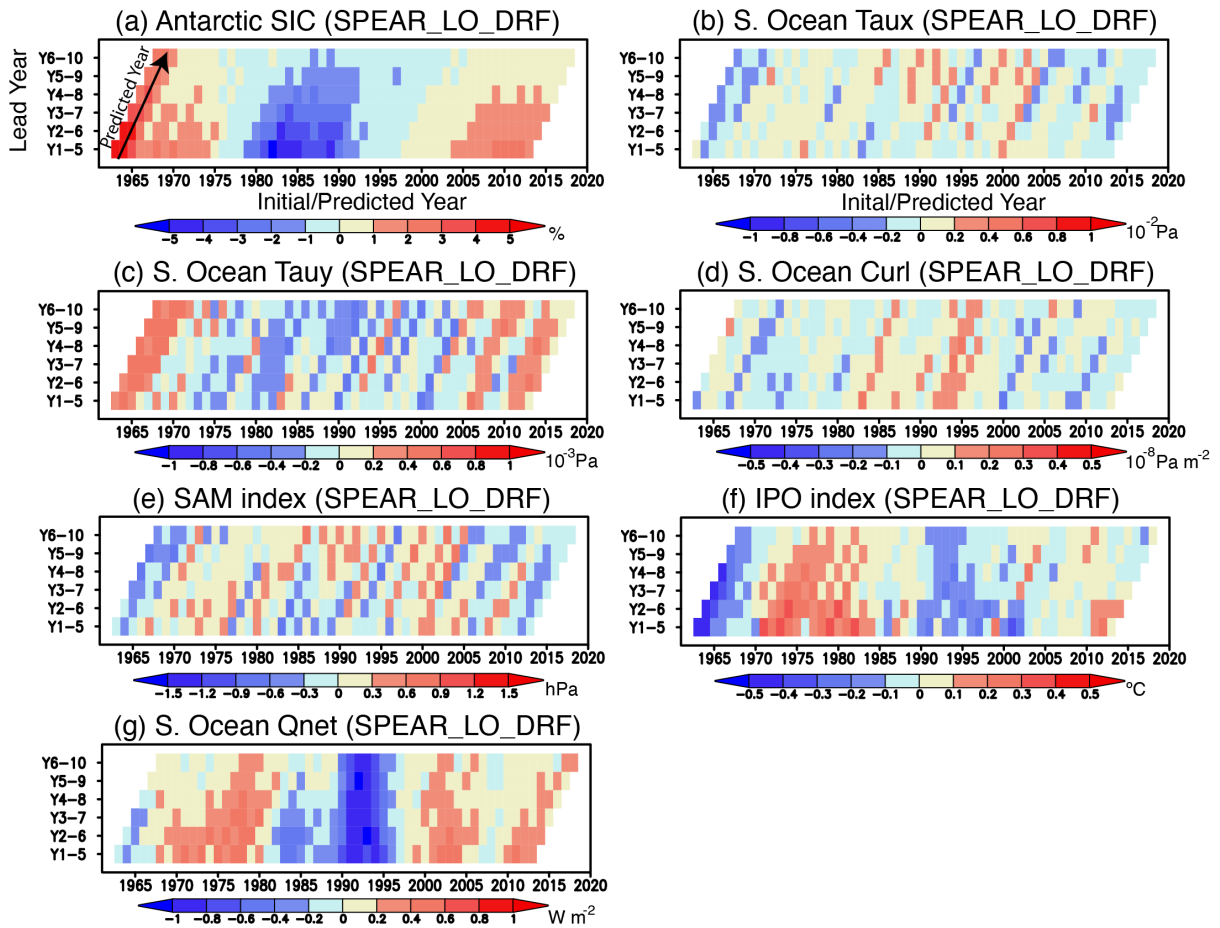
1170

1171

1172

1173

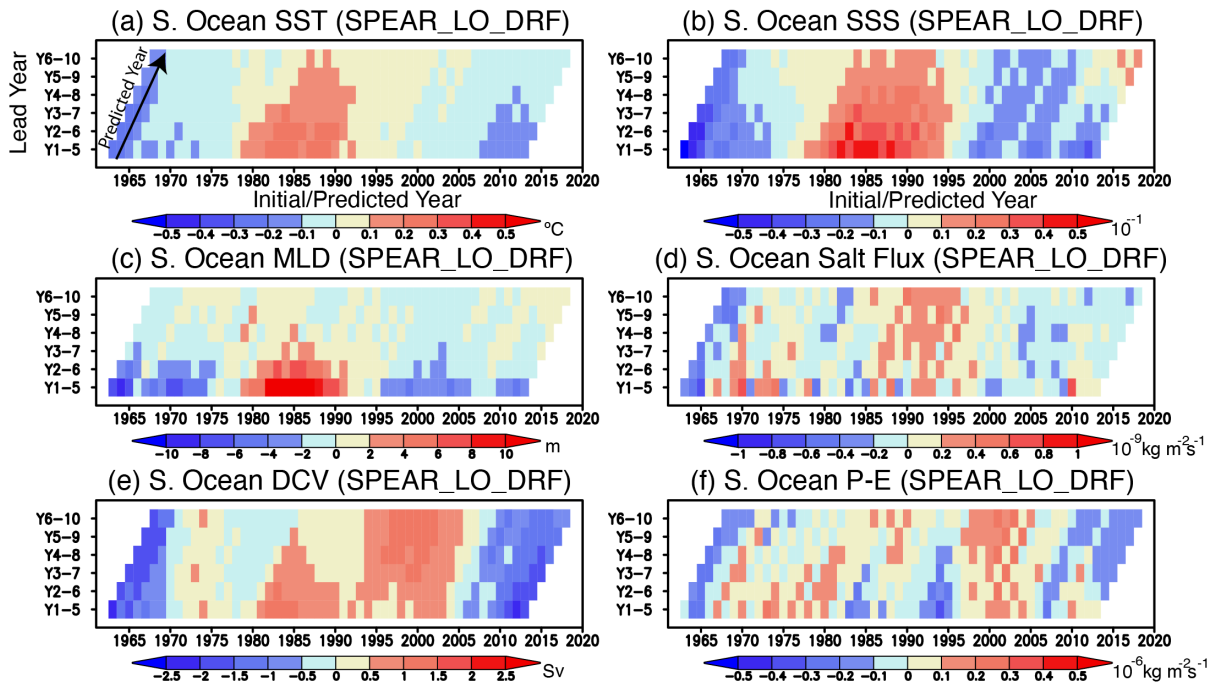
**Figure 9** (a) ACC and signal-to-noise (S/N) ratio of pan-Antarctic (area-weighted mean) SIC anomalies predicted at lead times from 1-5 years to 6-10 years. The ACCs from the persistence prediction (black) and the SPEAR\_LO\_DRF ensemble mean (ENS; red), which are statistically significant at 90 % using Student's *t*-test, are described with open circles. The average (AVG; blue) of individual ACCs from the SPEAR\_LO\_DRF is shown with its one standard deviation (shade in light blue). The S/N ratio from the SPEAR\_LO\_DRF (purple) is also plotted. (b) Same as in (a), but for the ACC and S/N ratio of the SIC anomalies averaged in the Weddell Sea. (c) Time series of 5-yr running mean pan-Antarctic SIC (in %) anomalies during 1961-2020. Black lines show the observed SIC anomalies from HadISST1 (solid) and HadISST2 (dotted), whereas other colored lines correspond to the ensemble mean SIC anomalies predicted at lead times from 1-5 years to 6-10 years in the SPEAR\_LO\_DRF. (d) Same as in (c), but for the SIC anomalies averaged in the Weddell Sea.



1174

1175 **Figure 10** (a) Temporal evolution of ensemble mean pan-Antarctic SIC anomalies predicted  
 1176 at lead times from 1-5 years to 6-10 years in the SPEAR\_LO\_DRF as a function of  
 1177 initial/predicted years (x-axis) and lead years (y-axis). A black arrow indicates the correlations  
 1178 with the same initial year for different lead times, while the corresponding x-axis indicates the  
 1179 predicted years. (b-d) Same as in (a), but for the zonal wind stress (Taux;  $10^{-2}$  Pa), meridional  
 1180 wind stress (Tauy;  $10^{-3}$  Pa), and wind stress curl (Curl;  $10^{-8}$  Pa  $m^{-2}$ ) anomalies averaged in the  
 1181 Southern Ocean (south of  $55^{\circ}$ S). Positive wind stress curl anomalies correspond to  
 1182 downwelling anomalies in the ocean. (e-f) Same as in (a), but for the SAM (in hPa) and IPO  
 1183 (in  $^{\circ}$ C) indices, respectively. (g) Same as in (b), but for the net surface heat flux anomalies (in  
 1184  $W m^{-2}$ ). Positive surface heat flux anomalies indicate more heat going into the ocean.

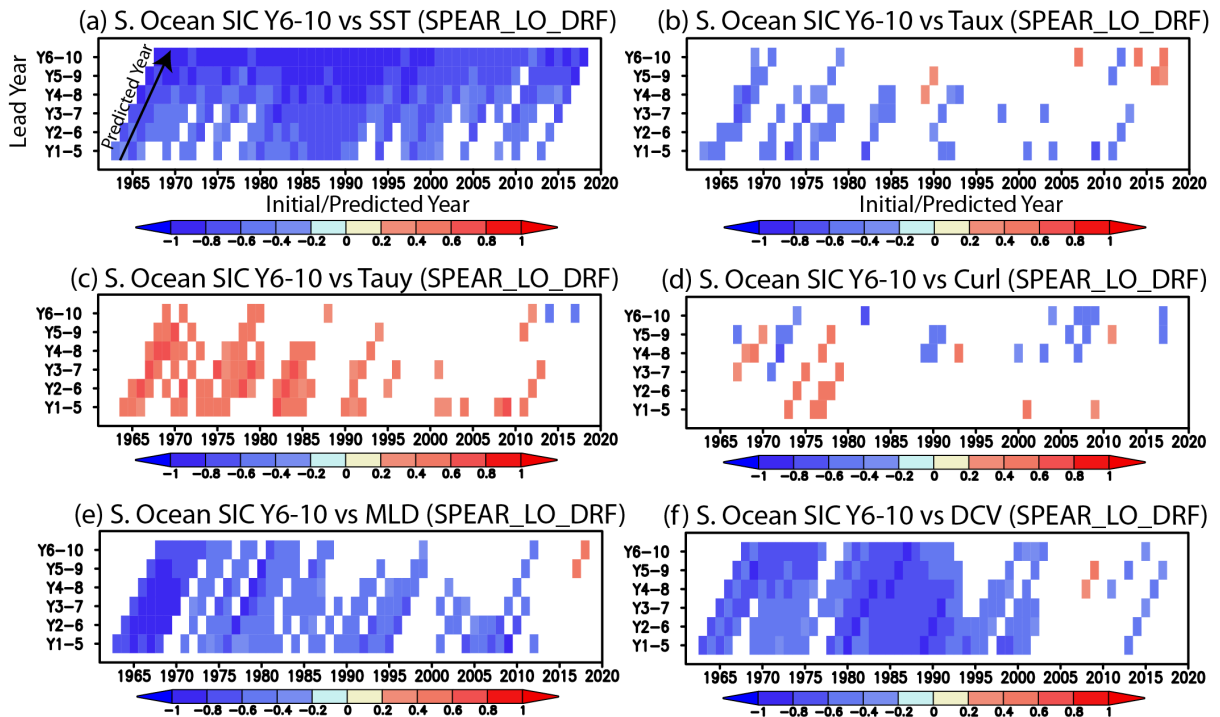
1185



1186

1187 **Figure 11** (a) Temporal evolution of ensemble mean Southern Ocean (south of 55°S) SST  
 1188 anomalies predicted at lead times from 1-5 years to 6-10 years in the SPEAR\_LO\_DRF as a  
 1189 function of initial/predicted years (x-axis) and lead years (y-axis). A black arrow indicates the  
 1190 correlations with the same initial year for different lead times, while the corresponding x-axis  
 1191 indicates the predicted years. (b-f) Same as in (a), but for the SSS (in  $10^{-1}$  PSU), mixed-layer  
 1192 depth (MLD; in m), salt flux (in  $10^{-9}$   $\text{kg m}^{-2} \text{s}^{-1}$ ), deep convection (DCV; in Sv), and  
 1193 precipitation minus evaporation (P-E; in  $10^{-6}$   $\text{kg m}^{-2} \text{s}^{-1}$ ) anomalies averaged in the Southern  
 1194 Ocean, respectively.

1195



1196

1197

1198

1199

1200

1201

1202

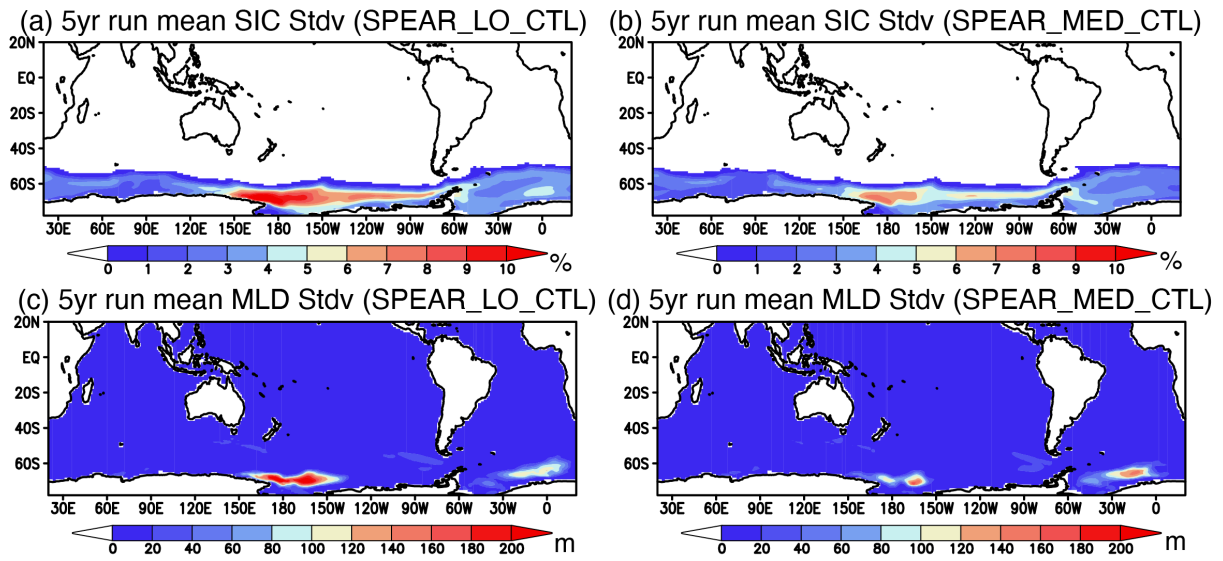
1203

1204

1205

1206

**Figure 12 (a)** Temporal evolution of inter-member correlation between the pan-Antarctic SIC anomalies predicted at a lead time of 6-10 years and the Southern Ocean SST anomalies predicted at lead times from 1-5 years to 6-10 years for the 20 ensemble members of the SPEAR\_LO\_DRF as a function of initial/predicted years (x-axis) and lead years (y-axis). A black arrow indicates the correlations with the same initial year for different lead times, while the corresponding x-axis indicates the predicted years. Correlation coefficients that are statistically significant at 90 % using Student's *t*-test are colored. **(b-f)** Same as in **(a)**, but for the inter-member correlation with the zonal wind stress, meridional wind stress, wind stress curl, mixed-layer depth, and deep convection anomalies averaged in the Southern Ocean.



1207

1208 **Figure 13** (a) Standard deviation of 5-yr running mean SIC (in %) anomalies from the  
 1209 SPEAR\_LO\_CTL with the preindustrial atmospheric radiative forcings. (b) Same as in (a), but  
 1210 for the SPEAR\_MED\_CTL. (c) Standard deviation of 5-yr running mean mixed-layer depth  
 1211 (MLD, in %) anomalies from the SPEAR\_LO\_CTL. (d) Same as in (c), but for the  
 1212 SPEAR\_MED\_CTL.

1213